Improved representation of volcanic sulfur dioxide depletion in Lagrangian transport simulations: a case study with MPTRAC v2.4

Mingzhao Liu[1], Lars Hoffmann[1], Sabine Griessbach[1], Zhongyin Cai[2], Yi Heng[3], and Xue Wu[4]

[1]Jülich Supercomputing Centre, Forschungszentrum Jülich, Jülich, Germany
[2]Yunnan Key Laboratory of International Rivers and Transboundary Eco-security, Institute of International Rivers and Eco-Security, Yunnan University, Kunming, China
[3]School of Computer Science and Engineering, Sun Yat-sen University, Guangzhou, China
[4]Institute of Atmospheric Physics Chinese Academy of Sciences: Beijing, Beijing, China

Correspondence: Mingzhao Liu (mi.liu@fz-juelich.de)

Abstract. The lifetime of sulfur dioxide (SO_2) in the Earth's atmosphere varies from orders of hours to weeks, mainly depending on whether cloud water is present or not. The volcanic eruption on Ambae Island, Vanuatu, in July 2018 injected a large amount of SO_2 into the upper troposphere and lower stratosphere (UT/LS) region with abundant cloud cover. In-cloud removal is therefore expected to play an important role during long-range transport and dispersion of SO_2. In order to better represent

5   the rapid decay processes of SO_2 observed by the Atmospheric InfraRed Sounder (AIRS) and the TROPOspheric Monitoring Instrument (TROPOMI) in Lagrangian transport simulations, we simulate the SO_2 decay in a more realistic manner compared to our earlier work, considering gas phase hydroxyl (OH) chemistry, aqueous phase hydrogen peroxide (H_2O_2) chemistry, wet deposition, and convection. The either newly developed or improved chemical and physical modules are implemented in the Lagrangian transport model Massive-Parallel Trajectory Calculations (MPTRAC) and tested in a case study for the July

10   2018 Ambae eruption. To access the dependencies of SO_2 lifetime on the complex atmospheric conditions, sensitivity tests are conducted by tuning the control parameters, changing the release height, predefined OH climatology data, the cloud pH value, the cloud cover and other. Wet deposition and aqueous phase H_2O_2 oxidation remarkably increased the decay rate of the SO_2 total mass, which leads to a rapid and more realistic depletion of the Ambae plume. The improved representation of chemical and physical ~~of~~ SO_2 loss processes described here is expected to lead to more realistic Lagrangian transport simulations of

15   volcanic eruption events with MPTRAC in future work.

1 Introduction

Volcanic eruptions have a strong impact on human living by causing various hazards and destructive impacts on human beings' living conditions. At the ground, SO_2 and acidic aerosols from eruption gases cause health hazards and increase respiratory morbidity and mortality (Hansell and Oppenheimer, 2004; Schmidt et al., 2011). The wet deposition of SO_2 leads to acid

20   precipitation that has a destructive effect on the ecosystem and environment, including acidifying the soil, contaminating the water sources and damaging the vegetation (Delmelle et al., 2002). In the UT/LS, sulfate aerosol formed by SO_2 oxidation has a significant impact on the radiative forcing and energy balance of the Earth by scattering solar radiation and by absorbing and

re-emitting thermal emissions (Robock, 2000; Kloss et al., 2020; Malinina et al., 2021). Satellite observations and atmospheric chemistry-transport modelling allow us to monitor the transport of volcanic ash and SO_2 and to better plan for evacuation and hazard mitigation. Studies on SO_2 long-range transport and dispersion can also help to better understand atmospheric dynamics, for instance the impact of the Asian monsoon on aerosol transport (Wu et al., 2017).

Remote sensing observations from satellite instruments are widely used assets to monitor and study volcanic activity. Satellite observations provide high-resolution SO_2 measurements on a global scale, which are particularly useful to initialize and evaluate the results of Lagrangian transport simulations. Among these instruments, the Atmospheric InfraRed Sounder (AIRS) (Aumann et al., 2003) and the TROPOspheric Monitoring Instrument (TROPOMI) (Veefkind et al., 2012) both provide data products that are capable of detecting volcanically enhanced SO_2 concentrations in the UT/LS. Hoffmann et al. (2014) proposed an SO_2 index based on brightness temperature difference for AIRS observations, which is most sensitive to SO_2 layers at 8 to 13 km and well suited to detect volcanic emission. The TROPOMI Level-2 SO_2 product provides volcanic SO_2 total column amounts for prescribed SO_2 plume heights at 1, 7, and 15 km with high horizontal resolution (Theys et al., 2020). These data products provide valuable references to evaluate and improve our transport model in the present study.

For the simulation of volcanic SO_2 transport, Lagrangian particle dispersion models are important tools that can resolve both small-scale features and long-range transport by calculating trajectories of ensembles of air parcels driven by deterministic (wind field and buoyancy) and stochastic (turbulence and convection) dynamics. In our past research, the Massive-Parallel Trajectory Calculations (MPTRAC) model (Hoffmann et al., 2016, 2022a) has been utilized to study volcanic eruption events, including research on source reconstruction (Heng et al., 2016; Cai et al., 2022), long-range transport (Wu et al., 2017, 2018), and large-scale parallel inverse modelling (Liu et al., 2020). Most of these studies predefined the SO_2 lifetime as a constant empirical value. However, the lifetime of SO_2 varies from orders of hours to weeks, depending on whether liquid or ice clouds are present or not (Eatough et al., 1994; McGonigle et al., 2004; Khokhar et al., 2005). In the gas phase, SO_2 is mainly depleted by reaction with OH, whereas in the presence of clouds SO_2 can be dissolved in cloud droplets and removed by precipitation or aqueous phase oxidation. Due to the variability of the complicated atmospheric background conditions, it is hard to use a specific number to represent the local SO_2 residence time. ~~Therefore~~

Various studies applied Lagrangian particle dispersion models for simulations of volcanic SO_2 plume transport. The study by Eckhardt et al. (2008) with the Flexible Particle (FLEXPART) model considered removal of SO_2 by reaction with OH radicals while aqueous-phase chemistry reactions were not considered. The study by de Leeuw et al. (2021) with the Met Office's Numerical Atmospheric dispersion Modelling Environment (NAME) model considered the conversion of SO_2 into sulfate aerosol with both gas phase and aqueous phase oxidation. In this work, we aim to model the ~~deposition~~ removal of SO_2 ~~with a more realistic~~ from volcanic plumes with representation of physical and chemical processes in the ~~framework of MPTRAC, including oxidation in the~~ MPTRAC model, including gas and aqueous phase ~~and wet deposition~~ ~~in this paper~~ oxidation as well as wet deposition. The chemical loss is represented by first-order rate coefficients derived from predefined, climatological OH and H_2O_2 fields. Chemistry calculations are conducted in the Lagrangian framework rather than using a Eulerian framework, which avoids memory sharing and is well suited for parallel processing. The approach achieves a balance between computational costs and accuracy, which is similar to the FLEXPART model but different from the full chemistry scheme applied in NAME.

Ambae Island (15.39°S, 167.84°E), located in the South Pacific in Vanuatu, contributed the largest volcanic eruption in the year 2018. Among four main eruption phases during 2017 and 2018, the most intensive one in July 2018 injected at least ~~4 × 10⁸~~ 400 ~~kg~~ kt of SO$_2$ to a peak altitude of ∼17 km (Moussallam et al., 2019). The volcanic SO$_2$ injected into the UT/LS formed aerosol particles that have a significant impact on atmospheric radiative forcing and global climate (Kloss et al., 2020; Malinina et al., 2021). ~~Compared with other~~ Other cases, e. g., the Raikoke eruption in 2019 (Cai et al., 2022; de Leeuw et al., 2021), Kasatochi in August 2008, Sarychev in June 2009 (Wu et al., 2017), and Nabro in June 2011 (Höpfner et al., 2015) ~~with SO$_2$~~ had lifetimes of about 14, 13, 24, and 32 days, ~~respectively~~ and SO$_2$ mass releases of 1500, 2000, 1200, and 3650 kt, respectively. Compared to these cases, the Ambae case in July 2018 ~~has~~ had a much shorter lifetime of ∼ 4 days (Malinina et al., 2021). Local reports of acid rain suggest that the eruption was accompanied by strong wet deposition, which means that the released SO$_2$ encountered significant wet removal. As we aim to better understand and represent these processes in the MPTRAC model, we selected the Ambae eruption in July 2018 as a case study for this work.

The paper is organized as follows. Section 2 introduces the updates on the chemical and physical modules in MPTRAC and provides a brief introduction to the AIRS and TROPOMI satellite observations. In Sect. 3, simulation results for the Ambae eruption in July 2018 are presented and evaluated, including the baseline simulation and various parameter sensitivity tests on the OH chemistry module, the H$_2$O$_2$ chemistry module, the wet deposition module, and the convection module. Section 4 provides the summary and conclusions of the study.

2 Data and methods

2.1 The MPTRAC Lagrangian transport model

For the simulation of the dispersion and depletion of SO$_2$ from the Ambae eruption, we applied the Massive-Parallel Trajectory Calculations (MPTRAC) model (Hoffmann et al., 2016, 2022a). Mainly, trajectories of air parcels are calculated by given horizontal winds and vertical velocities of meteorological input data, with additional stochastic perturbations being added to simulate diffusion and subgrid-scale wind fluctuations. Additionally, several improved or newly developed chemical and physical modules of MPTRAC are applied in the simulations. In particular, the SO$_2$ mass of the air parcels is decomposed by OH oxidation and wet removal processes instead of simply using an exponential decay with a fixed lifetime as applied in our earlier studies. The new and revised modules are described in the following sections.

The transport simulations with MPTRAC are driven by the European Centre for Medium-Range Weather Forecasts' (ECMWF's) fifth generation reanalysis ERA5 (Hersbach et al., 2020) with hourly meteorological data at $0.3° × 0.3°$ horizontal resolution on 137 vertical levels. This is a significant improvement in spatiotemporal resolution compared with the previous generation ERA-Interim reanalysis (Dee et al., 2011), providing only $0.75° × 0.75°$ horizontal resolution on 60 vertical levels at 6-hourly time intervals. The higher resolution ERA5 data are expected to lead to more accurate Lagrangian transport simulations compared to ERA-Interim (Hoffmann et al., 2019).

MPTRAC is a Lagrangian transport model, which is developed with a hybrid MPI-OpenMP-OpenACC parallelization scheme for application on CPU/GPU heterogeneous supercomputers, aiming for good parallel performance and scaling ef-

ficiency. The computing tasks in MPTRAC are distributed over the compute nodes and compute cores by MPI and OpenMP and offloaded to GPUs by means of OpenACC for faster and more energy-efficient computational performance (Liu et al., 2020; Hoffmann et al., 2022a). In this study, each individual simulation is conducted in parallel with 48 OpenMP threads. MPI parallel multi-processing for different model parameter settings is applied in the sensitivity tests, which significantly improves

95 the overall runtime of the simulations. On the state-of-the-art high performance computing system Jülich Wizard for European Leadership Science (JUWELS) at the Jülich Supercomputing Centre (Jülich Supercomputing Centre, 2019), individual Lagrangian transport simulations with 10^6 air parcels over a time period of 15 days require about 1.5 h of total runtime on a compute node. GPU acceleration was not considered here as there is no increase in computational speed at this problem size.

2.1.1 Hydroxyl radical oxidation in the gas phase

100 The hydroxyl radical (OH) is an important oxidant in the atmosphere, which causes rapid decay of many gas phase species. In MPTRAC, the mass decay of a trace gas of an air parcel is described by an exponential formula,

$$m(t + \Delta t) = m(t)\exp\left(-k\Delta t\right). \tag{1}$$

Assuming that the concentration of OH is in near steady-state, the pseudo first-order reaction coefficient k is calculated as

$$k = k_f \times [\text{OH}] \tag{2}$$

105 with an effective second-order coefficient k_f and a prescribed monthly zonal mean OH field. The oxidation of SO_2 with OH is a termolecular reaction,

$$SO_2 + OH \rightarrow [HOSO_2]^* \xrightarrow{M} HOSO_2, \tag{3}$$

where the excited intermediate $[HOSO_2]^*$ requires an inert molecule M (e. g., N_2 or O_2) to remove the energy and stabilize it into sulfate. In the high-pressure limit, the rate-limiting step is the production of $[HOSO_2]^*$, while in the low-pressure limit, the

110 reaction rate depends on the abundance of M and the production of $HOSO_2$. Thus, the effective second-order rate coefficient of the SO_2-OH oxidation process is temperature- and pressure-dependent, which is described here by using a formula given by the NASA Jet Propulsion Laboratory (JPL) data evaluation (Burkholder et al., 2019) as

$$k_f(T, [M]) = \frac{k_0(T)[M]}{1 + \frac{k_0(T)[M]}{k_\infty(T)}} 0.6^{\left\{1 + \left[\log_{10}\left(\frac{k_0(T)[M]}{k_\infty(T)}\right)\right]^2\right\}^{-1}}. \tag{4}$$

The high-pressure limit rate $k_\infty = 2.9 \times 10^{-31} \times \left(\frac{T}{298}\right)^{-4.1} \text{cm}^3 \text{molecule}^{-1} \text{s}^{-1}$ and the low-pressure limit rate $k_0 = 1.7 \times$

115 $10^{-12} \times \left(\frac{T}{298}\right)^{0.2} \text{cm}^6 \text{molecule}^{-2} \text{s}^{-1}$ were also obtained from the JPL evaluation.

As for the prescribed zonal mean OH fields, monthly mean climatology of OH calculated from simulation of the Chemical Lagrangian Model of the Stratosphere (CLaMS) is used by default (Pommrich et al., 2014). Another OH data set considered in this study was obtained from integrated the Copernicus Atmosphere Monitoring Service (CAMS) reanalysis OH data into monthly latitude- and pressure-dependent fields, keeping consistency with the CLaMS climatology (Inness et al., 2019). The

120 CLaMS data has 18 latitude bins and 34 pressure levels while CAMS data has 241 latitude bins and 25 pressure levels. CLaMS has a complete chemistry scheme on the stratospheric chemistry while the CAMS reanalysis uses a chemical mechanism most suitable for the troposphere. A comparison of the CLaMS and CAMS data sets with in-situ measurements is presented in the appendix. Whether the difference between the two OH datasets affects the MPTRAC simulations for the Ambae case study is discussed.

125 The formation of OH is driven by the photolysis of ozone in the troposphere and H_2O in the stratosphere, which causes a strong correlation with diurnal variability (Minschwaner et al., 2011). In contrast to previous versions of MPTRAC, which did not take diurnal variability into account, the mean OH climatology concentration $[OH]_0$ is multiplied here by a scaling factor depending on the solar zenith angle θ_{SZA} as proposed by Minschwaner et al. (2011) to model the diurnal variations,

$$f(\theta_{SZA}) = \exp[-\beta \sec(\theta_{SZA})]. \tag{5}$$

130 The term $\sec(\theta_{SZA})$ is the approximate air mass factor that represents the ratio of the optical slant path to the effective vertical path. The parameter β represents the vertical optical depth. Based on Minschwaner et al. (2011), a β value of 0.6 is used for simulations covering the UT/LS region. To maintain the same mean values of the scaled data as the monthly OH field, it is divided by a normalization factor that is obtained by integrating the correlation factor f over longitude λ. The final OH concentration is calculated as

$$135 \quad [OH] = \frac{[OH]_0 f(\theta_{SZA})}{\int_{-180}^{180} f(\theta_{SZA}(\lambda)) d\lambda / 360}. \tag{6}$$

Figure 1 shows average vertical profiles of the different OH data sets at tropical latitudes (from 23.5°S to 23.5°N). The CLaMS OH data (Pommrich et al., 2014), calculated using methane and ozone data taken from the HALOE climatology for the year 2005 (Grooß and Russell III, 2005), are compared with the CAMS OH reanalysis data for the years 2005 and 2018, respectively. The differences in the CAMS mean profiles between 2005 and 2018 are found to be negligible. Comparing the
140 CLaMS and CAMS OH data, these two datasets show similar concentrations in the troposphere while in the stratosphere, CLaMS OH concentrations are much larger than CAMS OH concentrations. To further evaluate the OH fields of the climatologies, we compared them to several NASA in-situ OH measurements in the troposphere at similar altitudes, solar zenith angles, and time periods and also to Microwave Limb Sounder(MLS) satellite data in the stratosphere. Both, CLaMS and CAMS data showed good agreement with the in-situ measurements in the troposphere. At altitudes above 20 km, CLaMS data show much
145 better agreement with MLS observations than the CAMS reanalysis. Further details of the comparison are presented in the appendix.

2.1.2 Hydrogen peroxide oxidation in the aqueous phase

The in-cloud oxidation pathway of SO_2 is mainly dominated by the reaction with hydrogen peroxide (H_2O_2),

$$\begin{aligned} SO_2 + H_2O &\rightleftharpoons H^+ + HSO_3^- \\ HSO_3^- + H_2O_2 &\rightarrow SO_4^{2-} + H^+ + H_2O \end{aligned} \tag{7}$$
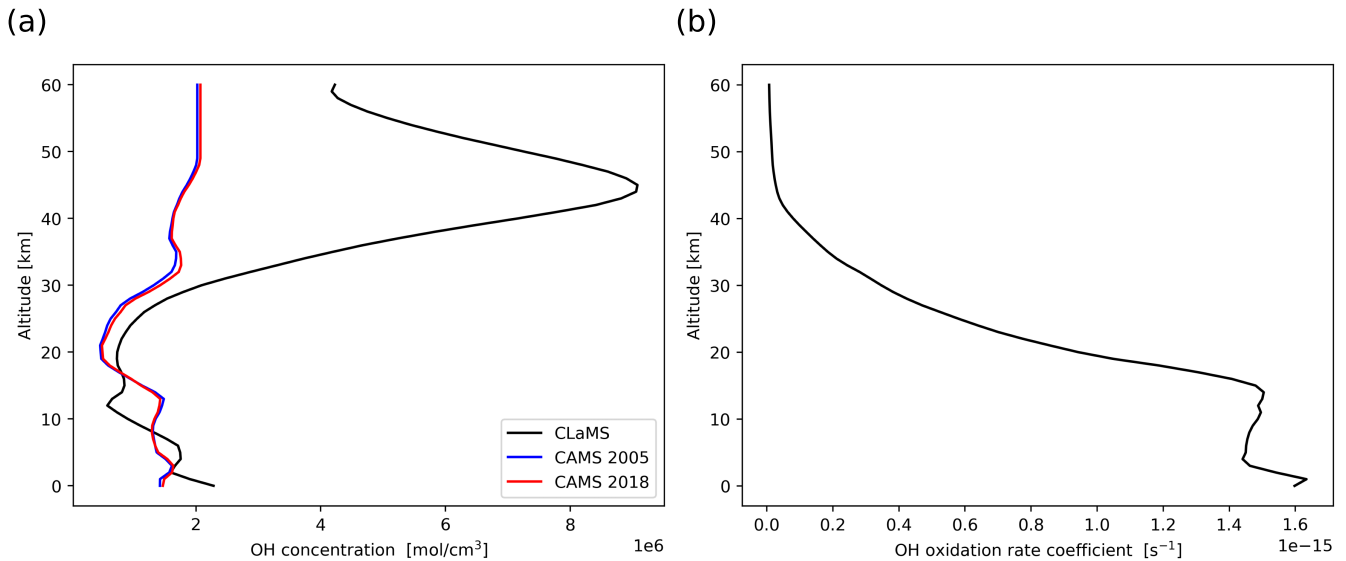
Figure 1. Vertical profiles of (a) OH concentrations over the tropics retrieved from CLaMS and CAMS climatology data, respectively, on 26 July 2018, 00:00 UTC and (b) OH oxidation rate coefficients at the same time.

150 Another oxide of SO_2 in liquid phase, ozone, is not considered here because its effects are expected to be negligible when $pH \leq 5$ (Rolph et al., 1992; Pattantyus et al., 2018). In contrast to OH, H_2O_2 has a longer atmospheric lifetime and cannot be treated as a static field as in the OH chemistry module. The reaction will rapidly deplete H_2O_2 in a few minutes (Pattantyus et al., 2018; Redington et al., 2009), keeping the H_2O_2 concentration in the aqueous phase much lower than equilibrium conditions from Henry's Law (Barth et al., 1989). To approximate the concentration of H_2O_2 in the aqueous phase, we use an

155 expression following Rolph et al. (1992) that is approximated from measurement data in Barth et al. (1989),

$$[H_2O_2]_{aq} = H_{H_2O_2} \times [H_2O_2]_g \times 0.59e^{-0.687[SO_2]_{vmr}} \tag{8}$$

Here, $H_{H_2O_2}$ represents the Henry's law constant of H_2O_2 (Sander, 2015). The concentration of H_2O_2 in the atmosphere is defined using monthly mean zonal mean data extracted from the CAMS reanalysis. The volume mixing ratio of SO_2 (in units of ppbv) is calculated in grid boxes of $1° \times 1°$ in the horizontal and 0.2 km in the vertical direction.

160 The concentration of the SO_2 in the aqueous phase is converted into a mass concentration in the air by multiplying the cloud water volume content L, thus the oxidation rate of SO_2 by H_2O_2 is formulated as (Rolph et al., 1992):

$$\frac{d[SO_2]_{aq}}{dt} = \frac{d[SO_2]_g/L}{dt} = -k_{H_2O_2}[H_2O_2]_{aq}K'H_{SO_2}[SO_2]_g. \tag{9}$$

Here, K' is the dissociation constant of H_2SO_3 (Berglen et al., 2004) and L is the volume liquid water content of the clouds. Combining Eqs. (8) to (9), the rate coefficient used in Eq. (1) of the H_2O_2 aqueous phase chemistry module is formulated as

165 $$k = k_{H_2O_2}[H_2O_2]_{aq}K'LH_{SO_2}. \tag{10}$$

The reaction rate coefficient $k_{\mathrm{H_2O_2}}$ is formulated as (Maass et al., 1999)

$$k_{\mathrm{H_2O_2}} = 9.1 \times 10^7 \times \exp\left[29700/R \times \left(\frac{1}{T} - \frac{1}{298.15}\right)\right]. \tag{11}$$

When the air parcel is located inside a grid box where the cloud water content is non-zero, the H_2O_2 oxidation scheme is activated to contribute to the depletion of SO_2.

170   In reanalysis data, cloud information always has uncertainties and cannot resolve finer scale cloud structures, which means that even in a cloudy grid box, the in-cloud oxidation may locally not take effect. Under this aspect, we implemented a control parameter allowing us to modify the cloud cover and to decrease the fraction of in-cloud oxidation. Only when a random number in the range of 0 to 1 is smaller than the given control parameter, the H_2O_2 chemistry will be activated. At present, the cloud cover default value is given as 0.8. In future versions of MPTRAC, the meteorological cloud cover can be used instead

175 of a pre-defined predefined value.

2.1.3 Wet deposition

Irreversible in-cloud and below-cloud wet removal processes of trace gases need to be treated separately. In MPTRAC, the cloud liquid water content (CLWC) and the cloud ice water content (CIWC) of the meteorological input data are used to determine whether an air parcel is located within or below a cloud. The total column cloud water c_l as well as the cloud depth

180 Z are additional input variables to the wet deposition module. Similar to Pisso et al. (2019), the precipitation rate P (in units of mm h^{-1}) is estimated from c_l (in units of kg m^{-2}) by means of a regression analysis using the ERA5 meteorological data for a region covering the Ambae eruption (10°S to 30°N, 160°W to 140°E) over the time period from 25 July to 31 July in 2018, as shown in Fig. 2,

$$c_l = 0.763 \times P^{0.478}. \tag{12}$$

185   For the modeling of in-cloud wet deposition, a similar exponential removal as in Eq. (1) is used with a scavenging coefficient Λ (in units of s^{-1}). The in-cloud wet deposition process is implemented with two schemes for a choice. The first scheme is based on the rain-out rate of cloud water, which determines the removal of a soluble trace gas taken up by cloud droplets and removal by precipitation according to the solubility of the trace gas. The in-cloud scavenging coefficient is calculated by multiplying the partition ratio of the species in the aqueous phase versus the gas phase α with the cloud water removal rate

190 (Slinn, 1974; Levine and Schwartz, 1982; Garrett et al., 2006),

$$\Lambda = \alpha \frac{P}{LZ}, \tag{13}$$

where L is the volume liquid water content of the cloud (in units of $m^3 \cdot m^{-3}$), Z is the depth of the cloud layer determined by the pressure of cloud top and cloud bottom as taken from the meteorological input data, and α is defined by

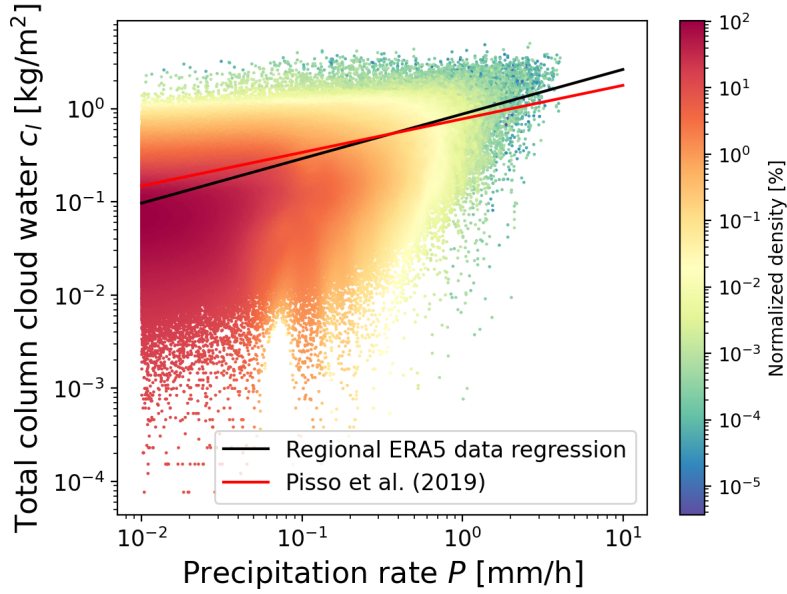$$\alpha = \frac{N_l}{N_g} = \frac{HP_xL}{P_x/\mathrm{R}T}, \tag{14}$$

Figure 2. Scatter density plot of total column cloud water versus precipitation rate of ERA5 meteorological data for a region and time period covering the Ambae eruption (see text for details). Color coding indicates the normalized density of the data points. The black line represents the regression of the data as given in Eq. (12). The ~~blue~~ red line shows the expression given by Pisso et al. (2019).

according to the ideal gas law, where H is Henry's law coefficient, R is the universal gas constant, and P_x is the partial pressure of species x.

Combining Eqs. (13) and (14), a formula similar to the approach of the HYSPLIT model (Draxler and Hess, 1998) is obtained,

$$\Lambda = \eta H \mathrm{R} T P Z^{-1}. \tag{15}$$

The factor η represents a temperature dependent retention coefficient in cloud versus equilibrium concentration in liquid water. The default value of η is set following Webster and Thomson (2014), assuming the cloud between 238.15 K to 273.15 K to be in the mixed phase, and a retention ratio in ice clouds to be 0.15:

$$\eta = \begin{cases} 1, & \text{if } T \geq 273.15\,\mathrm{K} \\ 0.15, & \text{if } T \leq 238.15\,\mathrm{K} \\ 0.15 + \frac{T - 238.15\,\mathrm{K}}{273.15\,\mathrm{K} - 238.15\,\mathrm{K}}(1 - 0.15), & \text{if } 238.15\,\mathrm{K} < T < 273.15\,\mathrm{K} \end{cases} \tag{16}$$

SO_2 is a moderate soluble gas with a Henry's Law constant of 1.3 M atm^{-1} at 298 K (Sander, 2015). However, the solubility of SO_2 strongly depends on the pH value because it undergoes dissociation. In the simulations for SO_2, the partition of SO_2 in clouds is represented by an effective Henry's law constant related to the pH value to account for the dissolution and dissociation

of SO$_2$ in cloud water (Berglen et al., 2004),

$$H_{\text{eff}}\left(\text{SO}_2\right) = H\left(\text{SO}_2\right) \times \left[1 + K'/\left[H^+\right] + K'K''/\left[H^+\right]^2\right]. \tag{17}$$

Here K' and K'' are the first and second dissociation constants of SO$_2$, using the formulation of Berglen et al. (2004), and $H\left(\text{SO}_2\right)$ is the Henry's law constant (Sander, 2015). With this method, the pH value becomes a control parameter of the model affecting the wet deposition, for which we assumed a default value of 4.5, guided by earlier work (Berglen et al., 2004; Koch et al., 1999).

For comparison, we also implemented another in-cloud wet deposition scheme applying an empirical exponential expression given by

$$\Lambda = \eta a P^b. \tag{18}$$

The choice of the parameters a and b follows the ~~UK Met Office's Numerical Atmospheric-dispersion Modelling Environment (NAME)~~ NAME model (Webster and Thomson, 2014).

The below-cloud wet deposition is a washout process through impact or diffusion with raindrops. With respect to SO$_2$, the washout rate has a typical magnitude of $\sim 10^{-5}\text{s}^{-1}$ (Maul, 1978; Martin, 1984; Elperin et al., 2015). Here, we set the parameters for SO$_2$ to $a = 2 \times 10^{-5}$ and $b = 0.616$, which follows the settings in the FLEXPART model (Pisso et al., 2019).

2.1.4 Convection

Due to the limited resolution of the global meteorological input data, neither ERA-Interim nor ERA5 are capable of resolving subgrid-scale convection processes. In MPTRAC, the extreme convection parametrization (Draxler and Hess, 1998; Gerbig et al., 2003) is used to represent the effects of convective up- and downdrafts being unresolved in the meteorological input data. The lifetime and depletion of SO$_2$ typically have a strong dependency on the atmospheric conditions at different altitudes. To test the impact of parametrized convection on the SO$_2$ transport simulations is part of the sensitivity tests presented this work.

The extreme convection parametrization requires the convective available potential energy (CAPE) and the height of the equilibrium level (EL) for input. CAPE represents the vertical atmospheric instability by integrating the local buoyancy of an air parcel from the level of free convection (LFC) to the EL,

$$\text{CAPE} = \int_{z_{\text{LFC}}}^{z_{\text{EL}}} g\left(\frac{T_{v,ap} - T_{v,env}}{T_{v,\text{env}}}\right) dz, \tag{19}$$

where $\text{T}_{v,ap}$ is the virtual temperature of the air parcel and $\text{T}_{v,env}$ is the virtual temperature of the environment. If the CAPE value is larger than a given threshold CAPE$_0$, an air parcel will be randomly redistributed between the surface and the equilibrium level, weighted by density. The method is similarly handled in the convective transport scheme in the Stochastic Time-Inverted Lagrangian Transport (STILT) model (Gerbig et al., 2003). A more detailed description and discussion of the calculation of the CAPE and EL values in MPTRAC is given by Hoffmann et al. (2022a).

2.2 Satellite data products

2.2.1 AIRS sulfur dioxide measurements

The Atmospheric InfraRed Sounder (AIRS) (Aumann et al., 2003) is an infrared spectrometer aboard the National Aeronautics and Space Administration's (NASA's) Aqua satellite. Aqua operates in a sun-synchronous low Earth orbit at orbit altitude of 705 km, providing nearly continuous measurements since September 2002. The AIRS instrument has across-track scanning capabilities. The swath width is 1780 km consisting of 90 footprints per scan with a footprint size of 13.5 km × 13.5 km at nadir. The measurements take place at about 01:30 and 13:30 local time for the descending and ascending sections of the orbits, respectively.

To detect the presence of volcanic SO_2 using the AIRS radiance measurements, an SO_2 index defined as the brightness temperature difference between 1407.2 cm^{-1} and 1371.5 cm^{-1} in the 7.3 μm SO_2 waveband is used (Hoffmann et al., 2014). The SO_2 index of Hoffmann et al. (2014) is most sensitive in the column density range of about 10 to 200 Dobson Units (DU) at altitudes of 8 to 13 km, which covers explosive volcanic eruptions with SO_2 injections into the UT/LS region. For SO_2 index values larger than 4 K, the SO_2 index is able to clearly detect volcanic plumes.

2.2.2 TROPOMI sulfur dioxide measurements

The TROPOspheric Monitoring Instrument (TROPOMI) (Veefkind et al., 2012) aboard the European Space Agency's Sentinel-5 Precursor satellite in a near-polar sun-synchronous orbit measures ultraviolet, visible, near-infrared, and shortwave infrared spectra at daytime. The TROPOMI instrument provides high spatial resolution with a pixel size of 7 km×3.5 km over a swath width of 2600 km.

The TROPOMI products include volcanic SO_2 abundances for prescribed plume heights of 1, 7, and 15 km, based on a detection algorithm described by Brenot et al. (2014) that recognizes enhanced SO_2 values from volcanic eruptions as well as anthropogenic sources. In this study, we use the TROPOMI Level 2 product with a priori SO_2 profiles centered around 15 km (Theys et al., 2017) for the time period of 24 July to 11 August 2018 during the Ambae eruption.

The SO_2 total mass of the Ambae eruption was calculated using the TROPOMI data to compare with the simulation results. TROPOMI scans the Ambae region at around 00:00 UTC. A grid with resolution of 0.1° covering the longitude range from 120°E to 110°W and the latitude range from 50°S to 30°N was used to calculate the average mass of SO_2 in each grid box and to sum up the total mass. A filter of θ_{SZA} <70° and the detection flag to filter out anthropogenic SO_2 were used for the analysis of the TROPOMI volcanic SO_2 data product as described in (Theys et al., 2020). The derived SO_2 total mass curve is very similar to the result of Malinina et al. (2021).

3 Results

3.1 Baseline simulation

In this section, we present a baseline simulation of the dispersion and depletion of the volcanic SO_2 plume of the Ambae eruption in July 2018. In our initial tests, it was found that with only OH oxidation and wet deposition being considered, the simulations cannot fully explain the observed fast depletion of SO_2. Therefore, we newly implemented the process of in-cloud oxidation with H_2O_2. As the plume transport in this case occurs in a high-CAPE tropical region, the convection module was also included. A CAPE threshold of $1000\,J\,kg^{-1}$ was used to include moderate to strong subgrid-scale convection in the baseline simulation. All the parameter settings in the baseline simulation use the default values as introduced in Sect. 2. In the following sections, we will ~~analyze~~ analyse the sensitivity of parameter choices for the ~~above mentioned~~ above-mentioned chemistry and physics modules of MPTRAC with respect to the baseline simulation setup.

Figure 3a shows the SO_2 total mass curve calculated from the TROPOMI data. The total mass of SO_2 in the UT/LS region shows a strong increase on 26 July 2018, reaching a peak on 28 July, and decreases back to pre-eruption levels on 7 August 2018. According to different satellite instrument observations of the Support to Aviation Control Service (SACS, 2022), the volcanic plume is detected directly over the volcano from 26 to 27 July. The bulletin report of the Global Volcanism Program (GVP) (Krippner and Venzke, 2019) states that the main explosion occurred on 26 July and another two intense episodes, producing volcanic lightning, occurred on 27 July. Based on the different satellite measurements, observational reports as well as empirical testing, we initialized the MPTRAC baseline simulation for the Ambae case study by releasing 10^6 air parcels with a total mass of ~~0.45~~450 ~~Tg~~ kt starting on 26 July, 00:00 UTC over the time period of 36 h, assuming a Gaussian vertical profile with the maximum centered at 14 km and a full width at half maximum (FWHM) of 4 km. Although there are more advanced methods available to accurately estimate the timing and vertical distribution of volcanic emissions (Hoffmann et al., 2016; Wu et al., 2017; Cai et al., 2022), we did not apply these techniques in this study because these techniques do not fully account for SO_2 chemistry. This study focuses on testing the new and revised chemical and physical modules and on conducting sensitivity tests with respect to the parameter choices. As discussed below, the baseline simulation with constant emission rate and Gaussian vertical profile represents the Ambae case reasonably well so that meaningful testing and evaluation can be conducted.

To properly assess the total mass evolution and the SO_2 plume patterns of the baseline simulation, the model output was sampled at the exact time and location as the TROPOMI satellite footprints ~~and output~~ by calculating the column density of all parcels located within a horizontal search radius of 7 km, as introduced in ~~Hoffmann et al. (2022a). Therefore, the sample output of the model can be directly compared and analyzed with the same perspective as the TROPOMI satellite observations~~Cai et al. (2022). Air parcels in data gaps of the satellite observations will ~~also~~ be excluded in the evaluation of the simulation results. The model results are multiplied by an altitude-dependent sensitivity profile, which was derived from TROPOMI averaging kernel data. The TROPOMI averaging kernel indicates full sensitivity above 10 km of altitude and the sensitivity only significantly decreases in the lower troposphere Cai et al. (2022). Since in this case most of the SO_2 injections and the plume height were located above 10 km, the inclusion of the averaging kernel does not significantly change the model

11

results . A lower threshold of ~~1.5~~ 1 Dobson units (DU) was applied to both the simulation data and the TROPOMI obser-
vations to eliminate the effects of noise. With this approach, the sample output of the model can be quantitatively analyzed
and compared with the TROPOMI satellite observations. As shown in Fig. 3a, the MPTRAC baseline simulation yields good
agreement with the total mass curve derived from the TROPOMI data. The overall SO_2 lifetime from the simulation is quite
similar to the observational data.

Figure 3b shows the relative mass loss with respect to the total emissions over time with regard to each module. At the end
of the simulation, OH chemistry, H_2O_2 chemistry and wet deposition lead to a mass loss of ~~46~~45%, 14%, and ~~26~~21% of the
total mass burden, respectively. The remaining mass loss in Fig. 3a is due to air parcels leaving the study region or having
SO_2 mass below the filtering threshold so that they are not accounted for in the mass budget anymore. The loss rates due to
in-cloud removal processes, including wet deposition and the aqueous phase H_2O_2 oxidation, strongly depend on the location
of the volcanic plume with respect to the cloud fields. The loss due to OH oxidation is a step-shaped curve due to the diurnal
variations of the OH concentration, leading to a faster loss rate at daytime and nearly zero loss at nighttime. ~~The loss rates~~
~~due to in-cloud removal processes, including wet deposition and the aqueous phase H_2O~~Simulations using an OH field with
diurnal variations will vary by 0.7% compared to using an OH field without diurnal variations. Differences are relatively low
in this case because the observations occur at about 13:00 local time. Overall, the diurnal variations of the OH field have little
effect on the SO_2 ~~oxidation, strongly depend on the location of the volcanic plume with respect to the clouds~~decay rates over
the entire simulation period, because the observational time scale is over several days and the diurnal variations are averaging
out.

Figure 4 shows comparisons of horizontal maps of the SO_2 plume from the baseline simulation with AIRS and TROPOMI
measurements, respectively. The bulk of the Ambae plume moved eastwards, and the moving speed is faster at lower altitudes.
A small plume at heights of 10 to 12 km moved northwards after 28 July at 160°W to 180°W, encountering strong wet
deposition. The model results match the satellite observations qualitatively well with similar location and shape of the plume.
At the end of the simulation the part of the plume under the cloud top has been almost depleted and the remaining part of
the plume above the cloud top somewhat shows deviations from the observations, which is attributed to unpolished temporal
and vertical variations of the emission estimates. Nevertheless, we consider the baseline simulation in its present form to be
suitable for further evaluation and sensitivity tests.

3.2 Sensitivity test on SO_2 release height

In this section, a series of simulations with air parcels released at different altitudes is presented to show the sensitivity of the
plume injection height on the evolution of SO_2 total mass burden. The tests use different release heights centered at 11, 13,
15, 17, and 19 km with 2 km wide uniform vertical distribution. The convection module was not activated in this test to avoid
vertical mixing of air parcels down to the surface during the simulations. As shown in Fig. 5, the SO_2 decay rate has an obvious
dependency on release height. Releasing the volcanic SO_2 at different heights leads to rather different horizontal spread and
different mass loss due to wet deposition, depending on whether the SO_2 plume encounters cloud regions or not.
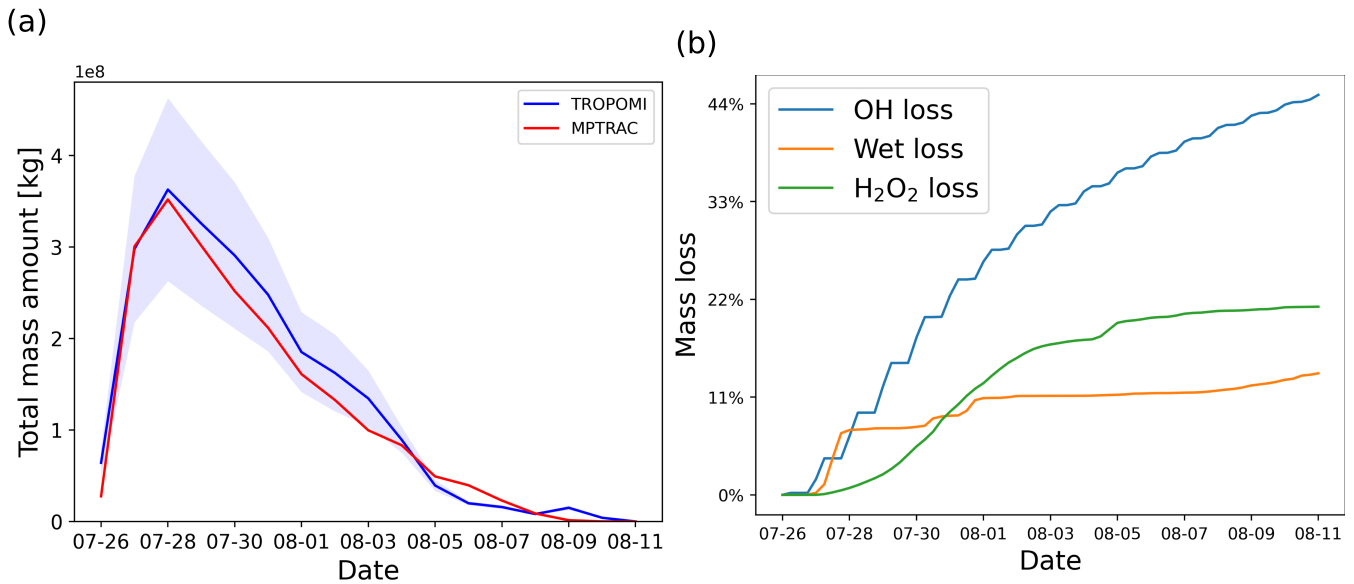
Figure 3. Observed (TROPOMI) and simulated (MPTRAC) SO₂ total mass curve (a) and mass loss (b) of the July 2018 Ambae eruption as a function of time. The blue shading represents the total error of the TROPOMI observations, combining random and systematic error components.

As shown in Fig. 5b, the mass loss due to wet deposition shows particularly high sensitivity to the release height. Wet deposition occurs mainly on 27 to 28 July when releasing air parcels at altitudes below 14 km, while most of the wet deposition mass loss occurs around 1 August when releasing above 14 km. Almost no wet deposition occurs above 18 km because it is above the tropopause and the maximum cloud top height. Aqueous phase H_2O_2 chemistry is most active at below 14 km, and has a strong sensitivity on release height, while above 14 km the H_2O_2 chemistry is very weak. The OH gas phase oxidation does not show a clear correlation with release height, with contributions to mass loss ranging from 30% to 60% of the total mass during the simulation. However, note that the OH concentrations and temperature- and pressure-dependent rate coefficients of the OH oxidation are not linearly increasing with altitude (compare Fig. 1) over heights from 10 to 20 km. Above 15 km, the OH oxidation rate decreases with height, while below 15 km, the decay rate is controlled mainly by in-cloud removal and the OH oxidation rate quickly decreases.

Figures 6 and 7 show the cloud top height and CAPE distributions derived from the ERA5 meteorological data as well as the particles released at different altitudes, clearly indicating which part of the plume is affected by wet removal and sub-grid convection, as distinguished by yellow and blue color. The plume released at the location of Ambae Island is transported to a region with high CAPE values and abundant clouds. The wet removal and subgrid-scale convection mainly take effect at altitudes below 15 km. The maximum CAPE values range approximately from 1000 to 1600 J kg^{-1}. In simulations with higher injection altitudes, the air parcels are transported mainly above the cloud top and are barely influenced by wet deposition and convection.

13
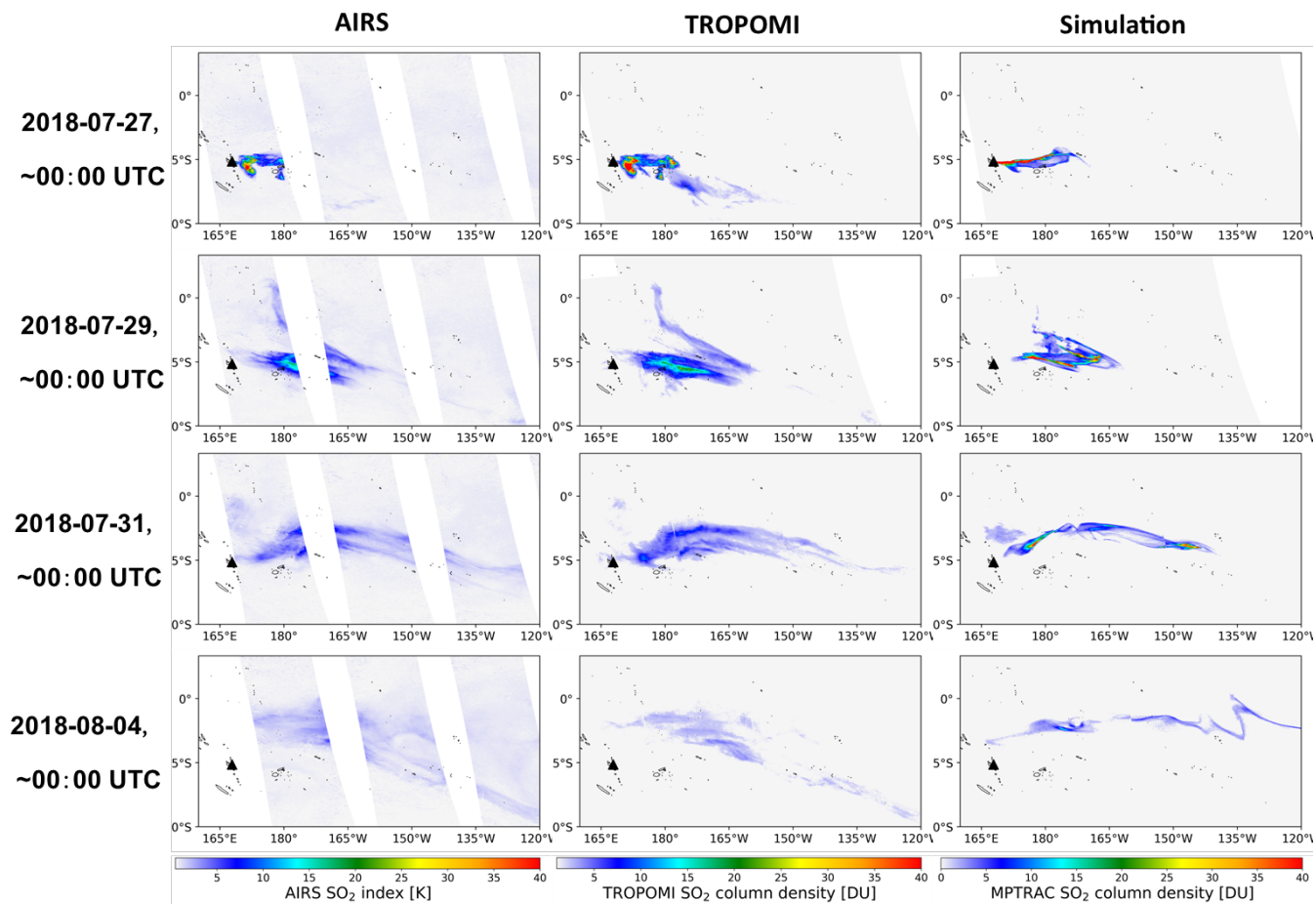
Figure 4. Evolution of the Ambae SO$_2$ plume in AIRS SO$_2$ observations (a) as well as column densities from TROPOMI observations (b) and MPTRAC simulations (c). The time of the satellite observations shown here was restricted to ± 3 h around 00:00 UTC. The black triangle shows the location of Ambae island. MPTRAC simulation results have been sampled on the TROPOMI footprints.

3.3 Sensitivity tests on OH chemistry

The SO$_2$ decay rate in the OH chemistry module is calculated by Eq. (2), which considers the temperature- and pressure-dependent reaction rate k_f and the OH concentration. The OH concentration is obtained from predefined monthly mean zonal mean data and the solar zenith angle correction to account for day- and nighttime conditions. The OH data used by default in MPTRAC is the monthly mean zonal mean climatology of Pommrich et al. (2014), which was calculated using the CLaMS model chemistry scheme. For another alternative, the CAMS global reanalysis provides 3-hourly OH data with a resolution of $0.75°$x$0.75°$. To reduce memory needs and maintain consistency with the CLaMS data approach, the CAMS data are also converted into monthly mean zonal mean data. To verify the impact of inter-annual differences, we compared the results between the simulations with CAMS reanalysis data for the years 2005 (matching the CLaMS data) and 2018 (matching the
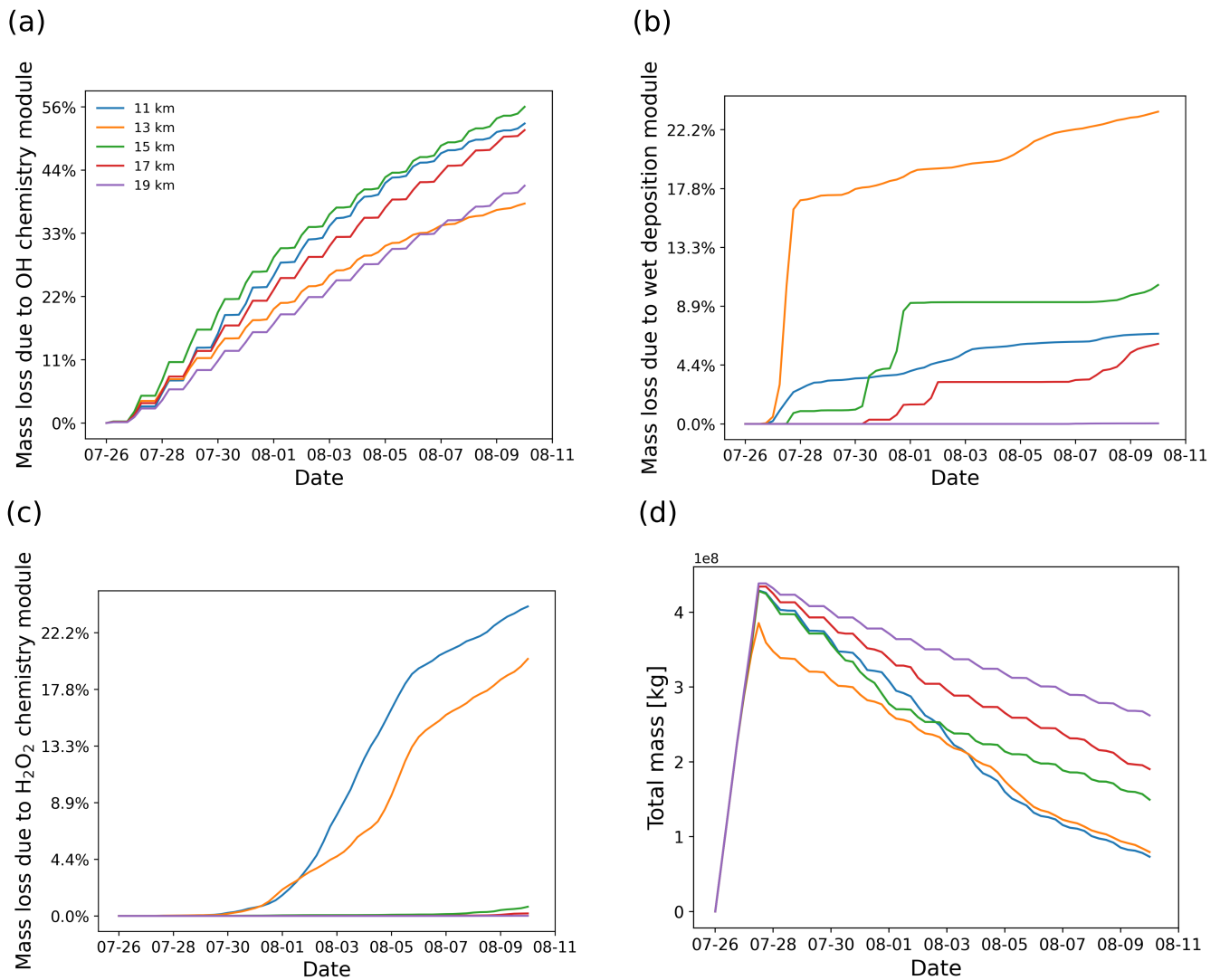
Figure 5. SO_2 mass loss with respect to the total mass (in percent) due to OH chemistry (a), wet deposition (b), and H_2O_2 chemistry (c) as well as total mass curves (d) derived from simulations that have different release heights centered at 11, 13, 15, 17 and 19 km.

Ambae eruption), respectively. For another test, simulations with regional CAMS OH data extracted from the longitude range from 160°E to 140°W are compared with global data.

As shown in Fig. 8, the inter-annual differences in the CAMS OH data are negligible (∼1 percentage point, pp). The differences between simulations with CAMS and CLaMS global OH data are ∼3 pp. The simulation with regional CAMS OH data for the location of the eruption has ∼4 pp difference compared with the global CAMS data. Overall, the inter-annual and regional differences of the OH data sets have a small influence on the amount of OH oxidation (less than 5 pp in this case),
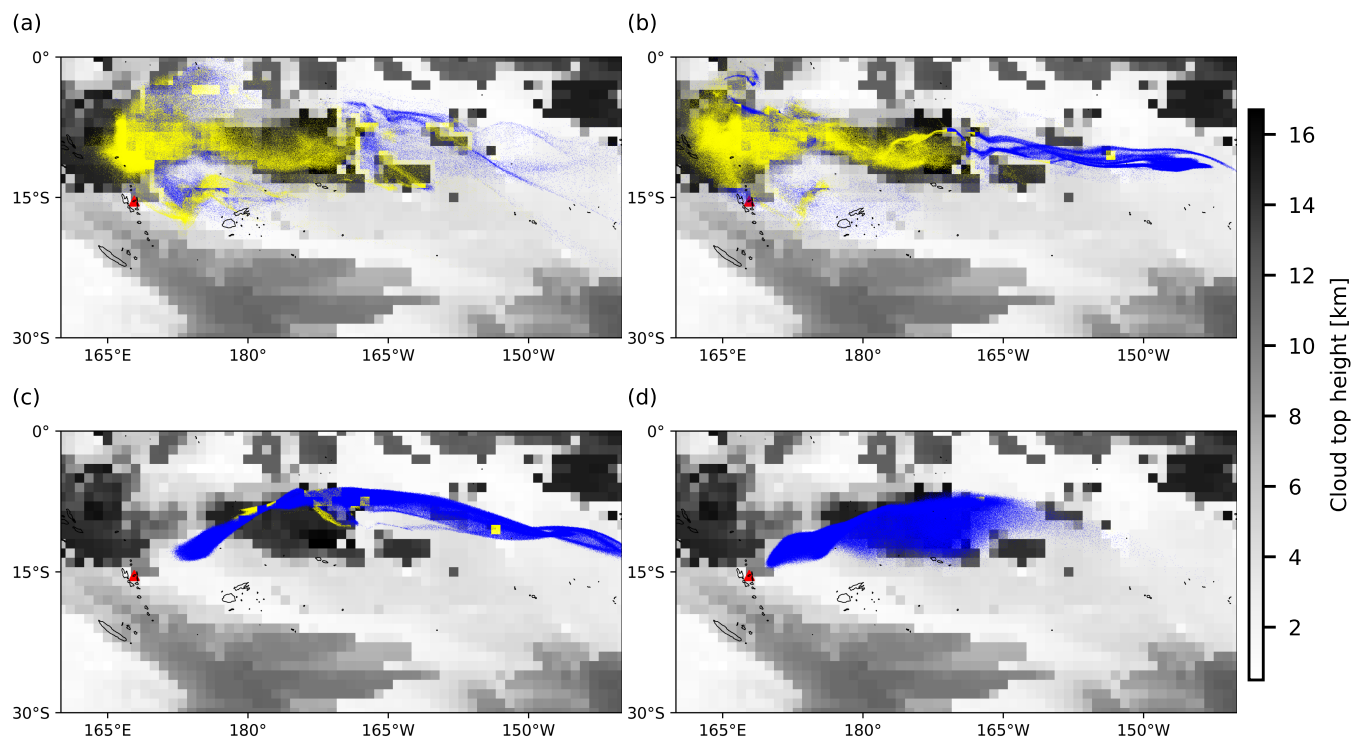
Figure 6. Background images represent the distributions of ERA5 cloud top height on 31 July 2018, 00:00 UTC. Dots represent air parcels that are released at altitudes of (a) 11 km, (b) 13 km, (c) 15 km, and (d) 17 km. A yellow dot indicates that the air parcel is below the cloud top height, triggering the wet deposition module, while a blue dot represents the opposite.

which suggests that using a monthly mean zonal mean climatology is a reasonable approach for modeling the OH loss of SO_2 in the UT/LS region.

3.4 Sensitivity tests on wet deposition

In the Ambae case study, the wet removal in clouds plays an important role in depleting SO_2 since the main plume passes through a cloud region. As introduced in Sect. 2.1.3, in-cloud wet deposition is handled as a rain-out process, which depends on the partition ratio of SO_2 in the cloud droplets and the precipitation rate. The partition ratio of SO_2 in liquid phase is defined with an effective Henry's law constant, depending on the assumed pH value. Here, we conducted a series of simulations to test the sensitivity to pH values in the range of 3 to 5, along with a comparison with the NAME wet deposition scheme (Webster and Thomson, 2014). As expected, higher cloud pH value lead to stronger wet deposition. The simulation with wet deposition according to the NAME scheme shows a similar deposition to the baseline simulation with the equilibrium scheme at pH 4 to 4.5. The difference between the two schemes is further reflected in the sensitivity with respect to convection, which will be discussed in Sect. 3.6
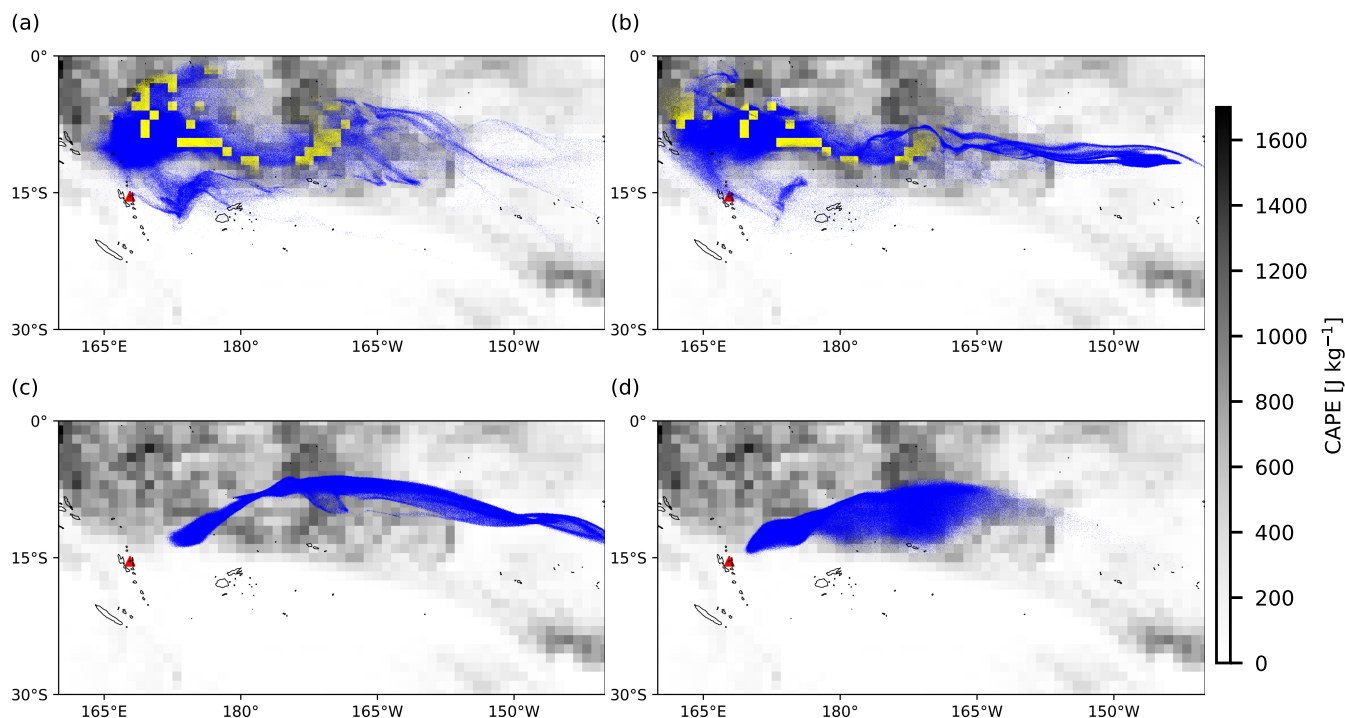
Figure 7. Same as Fig. 6, but background images represent the distribution of ERA5 CAPE values on 31 July 2018, 00:00 UTC. Yellow dots indicate air parcels below the equilibrium level and local CAPE values larger than $1000 \, \mathrm{J \, kg^{-1}}$, triggering the convection module, while blue dots represent the opposite.

The retention ratio represents the solute species in the ice phase versus that in the liquid hydrometeor. The retention coefficient may vary depending on temperature, pH, ventilation rate, accretion rate, and impact velocity (Stuart and Jacobson, 2006). Laboratory studies on the retention ratio of SO_2 suggest a range from 1% to 60% (Iribarne et al., 1983; Lamb and Blumenstein, 1987; Iribarne et al., 1990). As introduced in Sect. 2.1.3, a retention coefficient dependent on temperature is applied to model the differences of wet deposition in ice and liquid cloud. Figure 10 shows the SO_2 mass loss curves of simulations given different retention ratios in the range of 0.01 to 1. In this case, most of the wet deposition occurs in ice clouds leading to a strong dependency on the retention ratio.

3.5   Sensitivity tests on H_2O_2 chemistry

Since the meteorological data cannot fully resolve the convection and detailed cloud structures, a parameter cloud cover was defined in the H_2O_2 chemistry module to represent the probability of an air parcel to be located in a cloud. When a random number in the range of 0 to 1 is larger than a given threshold for the cloud cover, the H_2O_2 decomposition will be skipped. Figure 11 shows the dependency of aqueous phase H_2O_2 oxidation on cloud cover. Compared to full cloud cover, the amount

17
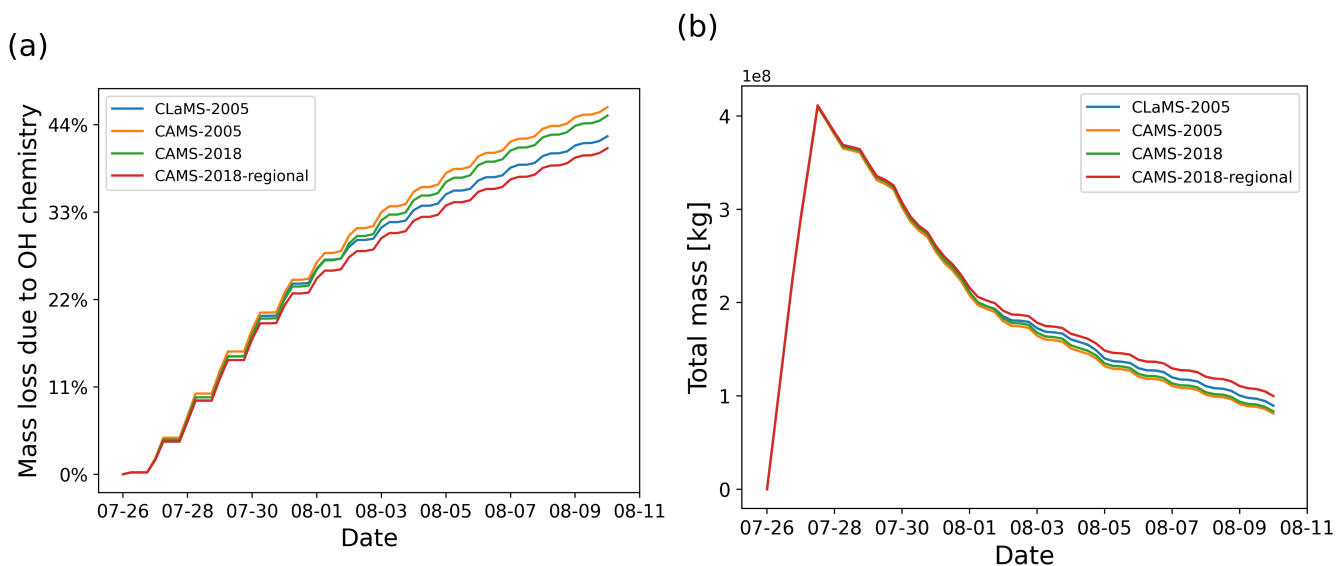
Figure 8. SO$_2$ mass loss with respect to total mass (in percent) due to the OH chemistry module (a) and total mass curves (b) for simulations with different OH datasets, including CLaMS data in 2005, CAMS data in 2005 and 2018, and CAMS regional data in 2018 (see text for details).
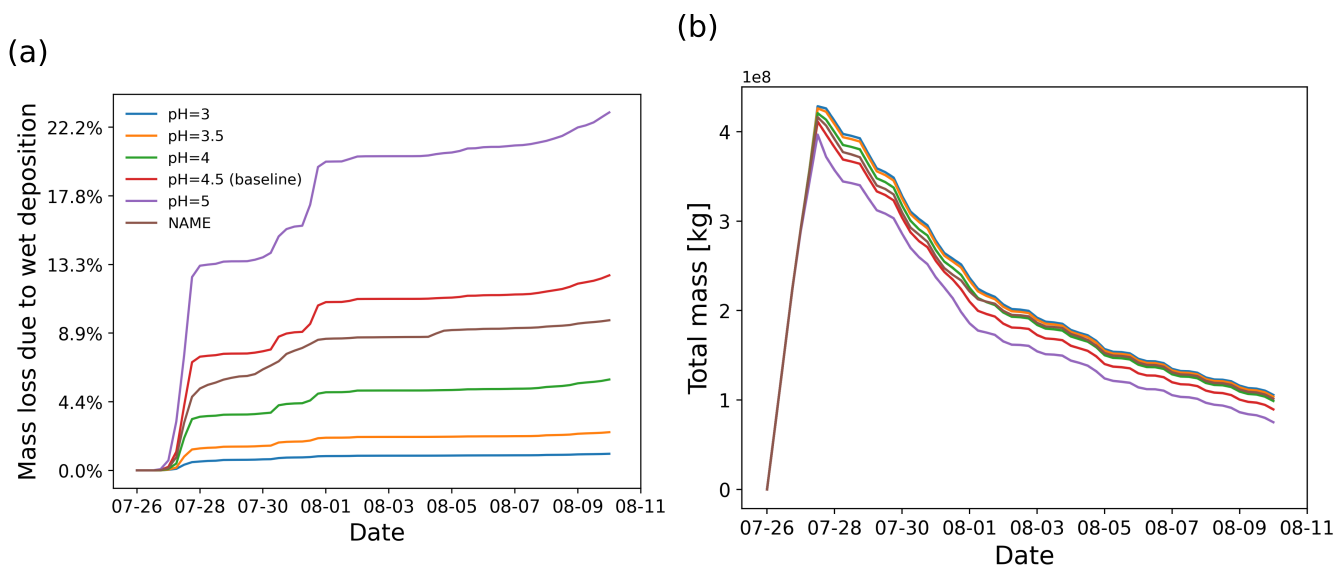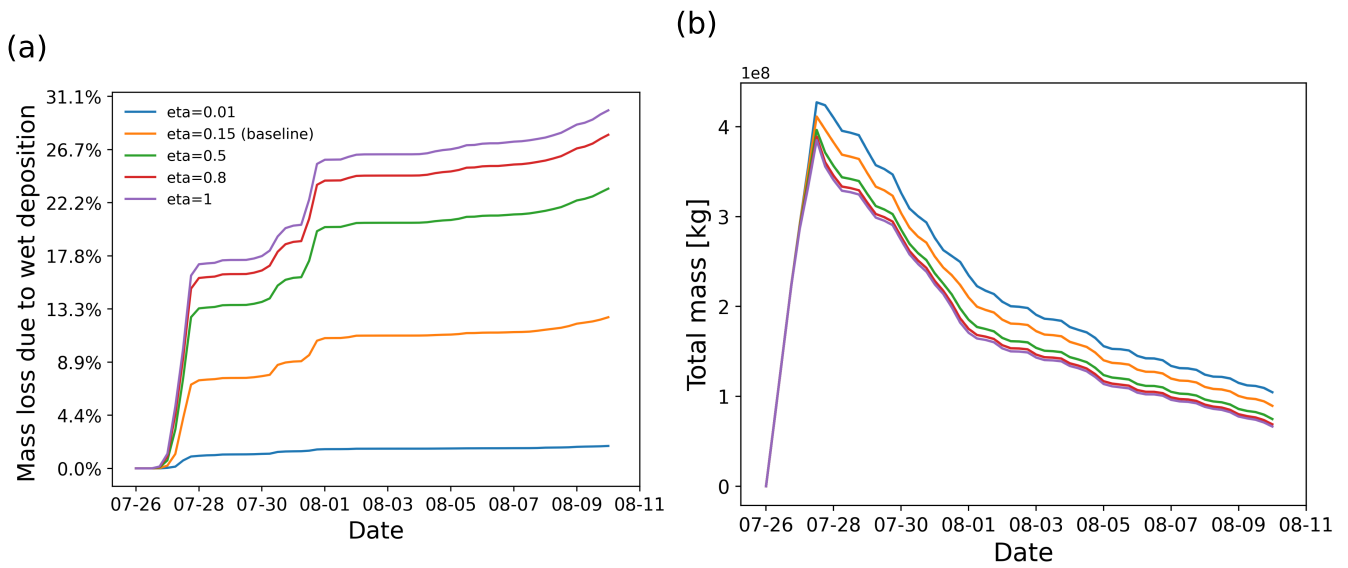

Figure 9. SO2 mass loss with respect to total mass (in percent) due the wet deposition module (a) and total mass curves (b), derived from simulations that use different pH values in the wet deposition module and comparing with the wet deposition scheme of the NAME model.

Figure 10. SO2 mass loss with respect to the total mass (in percent) due the wet deposition module(a) and total mass burden evolution (b), derived from different simulations that use different retention ratios settings in the wet deposition module.

of H_2O_2 oxidation in a case with only 10% cloud cover is decreased by 8 pp. However, the SO_2 total mass burden is only slightly ~~change~~changed.
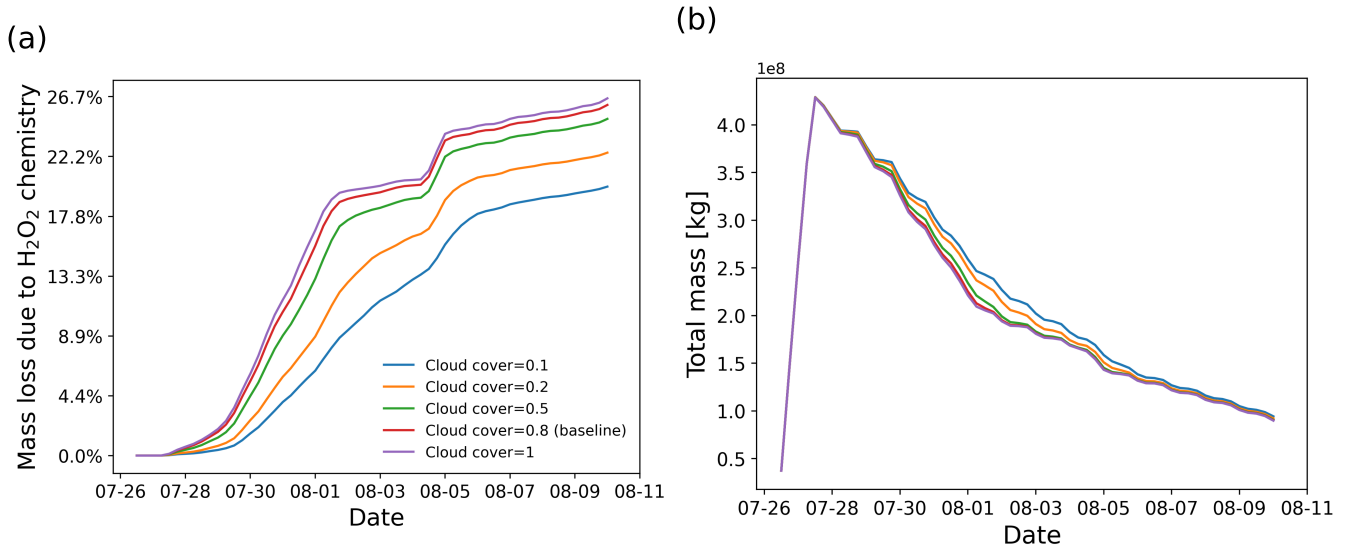
Figure 11. SO2 mass loss with respect to total mass (in percent) due the H_2O_2 chemistry module (a) and total mass burden evolution (b), derived from simulations that use different cloud cover settings in the H_2O_2 chemistry module.

3.6 Impact of the extreme convection parametrization

Due to better spatiotemporal resolution, the ERA5 meteorological data provide more accurate information than ERA-Interim to resolve mesoscale features (Hoffmann et al., 2019). However, convective up- and downdrafts are still underrepresented in the ERA5 data. In MPTRAC, the extreme convection parametrization is applied to represent the effects of unresolved convection in the meteorological input data. In convective columns, the convection module will randomly redistribute the air parcels between the surface and the equilibrium level, if CAPE exceeds a given threshold $CAPE_0$. As shown in Fig. 7, the SO_2 plume released by the Ambae volcanic eruption was transported to a high CAPE region which makes it a valuable case to study the potential effects of unresolved convection. In this section, the effects of parametrized convection for different thresholds $CAPE_0$ will be discussed.

Figure 12 ~~a~~ shows the vertical distributions of the SO_2 mass of the Ambae plume for different thresholds $CAPE_0$ from 0 to 2000 J kg^{-1}. The case of $CAPE_0$ being zero represents the extreme case in which convection occurs everywhere below the equilibrium level where CAPE is present. For $CAPE_0$ larger than 1000 J kg^{-1}, the parametrized convection is restricted to represent moderate to strong convective events only. There is almost no additional convection for $CAPE_0$ larger than 2000 J kg^{-1} compared to the case without parametrized convection. When applying a larger $CAPE_0$, more air parcels will be transported to altitudes below the equilibrium level ($\sim$14 km).

Figure 13 shows the impact of parametrized convection on mass loss in the SO_2 transport simulations for the Ambae case. The largest sensitivity is found for the H_2O_2 oxidation, while OH oxidation and wet deposition show little difference. This is because some air parcels are transported to heights below 14 km where the H_2O_2 oxidation is most active. The H_2O_2 chemistry is much more sensitive to height than the OH chemistry and wet deposition at altitudes where convection occurs (see Sect. 3.2). Regarding the mass evolution, the effect of the convection module enhances the depletion of SO_2 below the cloud top. At the end of simulation, most of the remaining SO_2 is above cloud top where the convection module takes no effect.

4 Discussion and conclusions

We present recent improvements of the chemical and physical modules in the Lagrangian transport model MPTRAC for simulating the dispersion and depletion of SO_2 from volcanic eruptions. The improved modules include gas phase OH oxidation, aqueous phase H_2O_2 oxidation, wet deposition, and parametrized convection. In a case study, the modules are applied for simulations of the SO_2 plume evolution of the Ambae eruption in July 2018. We present a baseline simulation, in which the modeled mass evolution shows a good match with TROPOMI satellite observations.

In our simulations, the implementation of wet deposition and H_2O_2 oxidation significantly decreased the lifetime of SO_2 in clouds. Gas phase oxidation by OH, aqueous phase oxidation by H_2O_2, and wet deposition remove about ~~46~~45%, 14%, and ~~26~~21% of the SO_2 total mass burden during a simulation time period of 15 days, respectively. Based on the baseline simulation, a series of sensitivity tests was conducted by tuning various control parameters of the modules to better understand the impacts of the chemical and physical processes on SO_2 dispersion. Initially, we tested the sensitivity on the assumed injection height of the SO_2 plume. The SO_2 plume undergoes much faster depletion below 14 km in clouds than in the dry
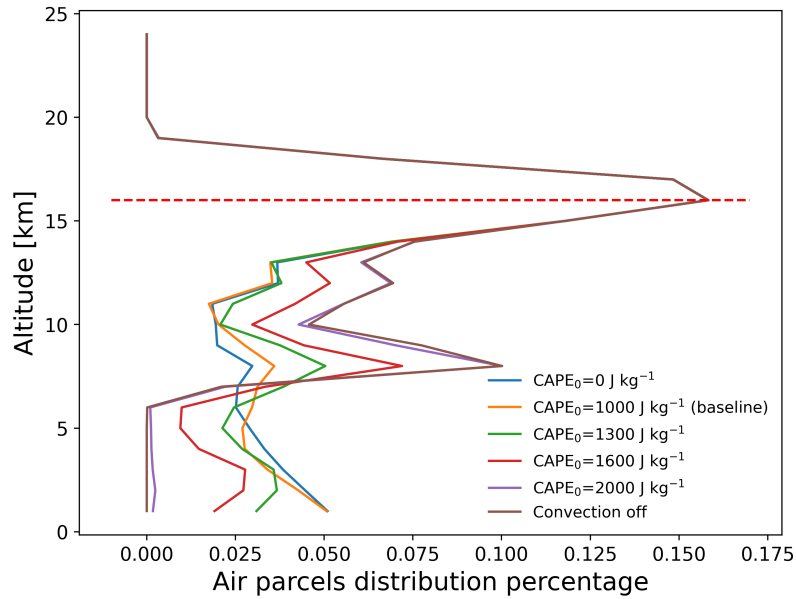
Figure 12. Vertical distribution of total SO_2 mass of the air parcels on 1 August 2018, 00:00 UTC from simulations with different CAPE thresholds. The red dashed line ~~represents~~ indicates the ERA5 thermal tropopause height ~~of~~ over the ~~tropopause~~Ambae region (Hoffmann and Spang, 2022).

atmosphere because rain-out processes and aqueous phase oxidation are bound to the presence of clouds. Variations of cloud distributions and vertical wind shear lead to rather different amount of wet deposition and aqueous phase oxidation for different injection heights.

425   For the OH chemistry module, different OH monthly mean zonal mean concentration data sets have been tested. It was found that the differences in mass loss between different OH datasets (CAMS versus CLaMS, regional versus global, and year 2005 versus 2018) are limited (less than 5 pp of the total mass). Using a monthly mean zonal mean climatology of OH for simulating SO_2 mass loss over time is considered a suitable approach for transport simulations covering the UT/LS region. For wet deposition, an analytic solution derived for the rain-out process according to Henry's law is considered in cloud.

430 The assumed pH value of the effective Henry's Law constant for SO_2 has a strong effect on the amount of wet removal of SO_2. Compared with the wet deposition scheme with a scavenging coefficient formula applied in the UK Met Office's NAME model, our simulation at an assumed pH value of 4.5 yields a similar level of wet deposition. The impact of the retention ratio of the soluble gas in ice cloud is also discussed. Due to the low temperatures in the UT/LS region, most of the regions affected by the Ambae eruption are covered with ice clouds. Therefore, the amount of wet deposition strongly depends on

435 the assumed retention ratio. For H_2O_2 chemistry in the aqueous phase, the impact of cloud cover has been tested. By tuning the CAPE threshold used in the extreme convection parametrization, the vertical distribution of the SO_2 plume might be strongly altered, which in turn will impact the depletion of SO_2. It is found that aqueous phase oxidation via H_2O_2 is mostly
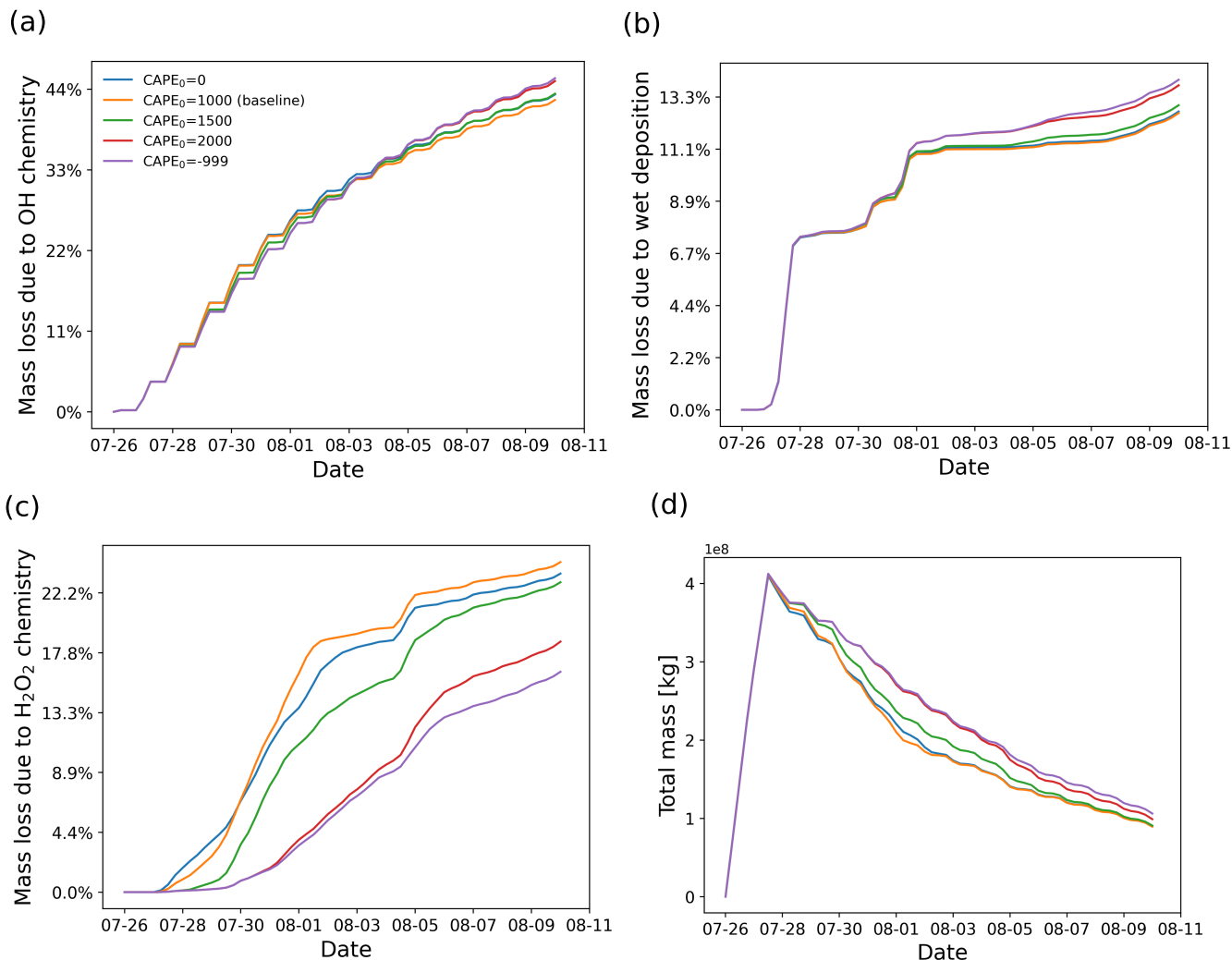
Figure 13. Same as Fig. 5, but derived from simulations with different CAPE thresholds in the convection module.

~~affected~~ influenced, whereas wet deposition and OH oxidation are not so sensitive to the vertical redistribution of the air parcels due to the parametrized convection.

440   In this study, we improved the Lagrangian transport simulations of volcanic SO_2 with MPTRAC by implementing more realistic physical and chemical process representations instead of using an exponential decay law with a fixed lifetime as in our earlier studies. However, the refinements on the modeled loss processes lead to a high sensitivity to the release vertical profile and cloud abundance. The backward trajectory method developed to estimate time- and height-resolved SO_2 emissions with MPTRAC (Hoffmann et al., 2016; Wu et al., 2017) is currently incapable of taking into account the additional complexity

445   of the revised chemistry and wet deposition parametrizations. In future work, we plan to implement a more advanced inverse

22

modeling techniques for MPTRAC to reconstruct the initial SO_2 injections of volcanic eruptions, which can take the model improvements described here into account.

The representation of volcanic SO_2 depletion in different atmospheric conditions above and below the cloud top in the current MPTRAC scheme considers first-order loss processes to estimate rate coefficients and lifetimes. In reality, the chemical

450   processes affecting the lifetime of volcanic SO_2 may be more complicated. Large-scale emissions of volcanic SO_2 into the atmosphere will reduce the abundance of atmospheric oxides. The scattering and reduction of solar radiation by ash and other aerosol particles will reduce the photochemical regeneration of the oxides. Other factors, such as additional water release from an eruption or absorption by volcanic ash, need to be further investigated to better understand and elucidate the mechanism of their dynamics. In future work, we intend to further test and improve the current version of MPTRAC to explore its applicability

455   to other volcanic eruption cases.

Appendix A: Validation of OH fields with diurnal variability

A monthly mean zonal mean OH climatology with diurnal corrections according to Eq. (6) is used as input to calculate the decomposition of SO_2 due to OH oxidation. For validation of the OH data, we extracted OH values from MPTRAC as a function of the solar zenith angle and compared them with in-situ measurement data provided by the NASA Earth Science

465   Project Office (ESPO, 2022). Here, we present comparisons for April (Fig. A1) and October (Fig. A2) containing in-situ measurements of campaigns SUCCESS-DC8, SONEX-DC8, POLARIS-ER2, and MAESA-ER2, covering altitudes ranging from 5 to 21 km. For the stratosphere, a comparison with OH data from MLS is shown in Fig A3. It is found that CLaMS OH data better represent the measured OH concentrations than the CAMS reanalysis in the stratosphere. For the troposphere, the OH data from CLaMS and CAMS both match the measurements well.
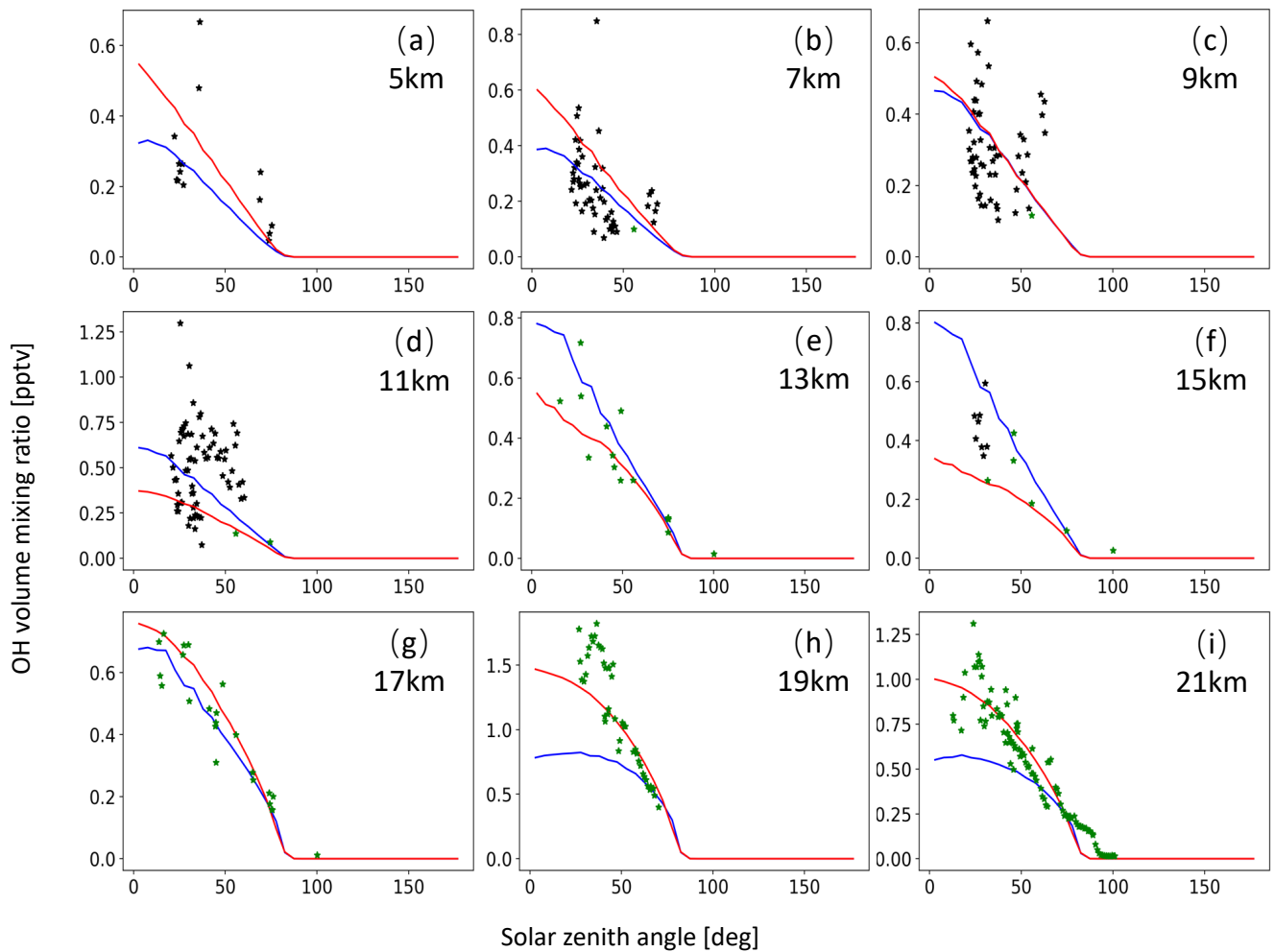
Figure A1. OH volume mixing ratios used for MPTRAC based on predefined monthly mean zonal mean data for the CLaMS model (red curve) and the CAMS reanalysis (blue curve) as well as OH in-situ measurements from the campaigns SUCCESS-DC8 (black points) and POLARIS-ER2 (green points). The time period being covered is the month of April. Plots in (a) to (i) refer to altitudes of 5, 7, 9, 11, 13, 15, 17, 19, and 21 km, respectively.
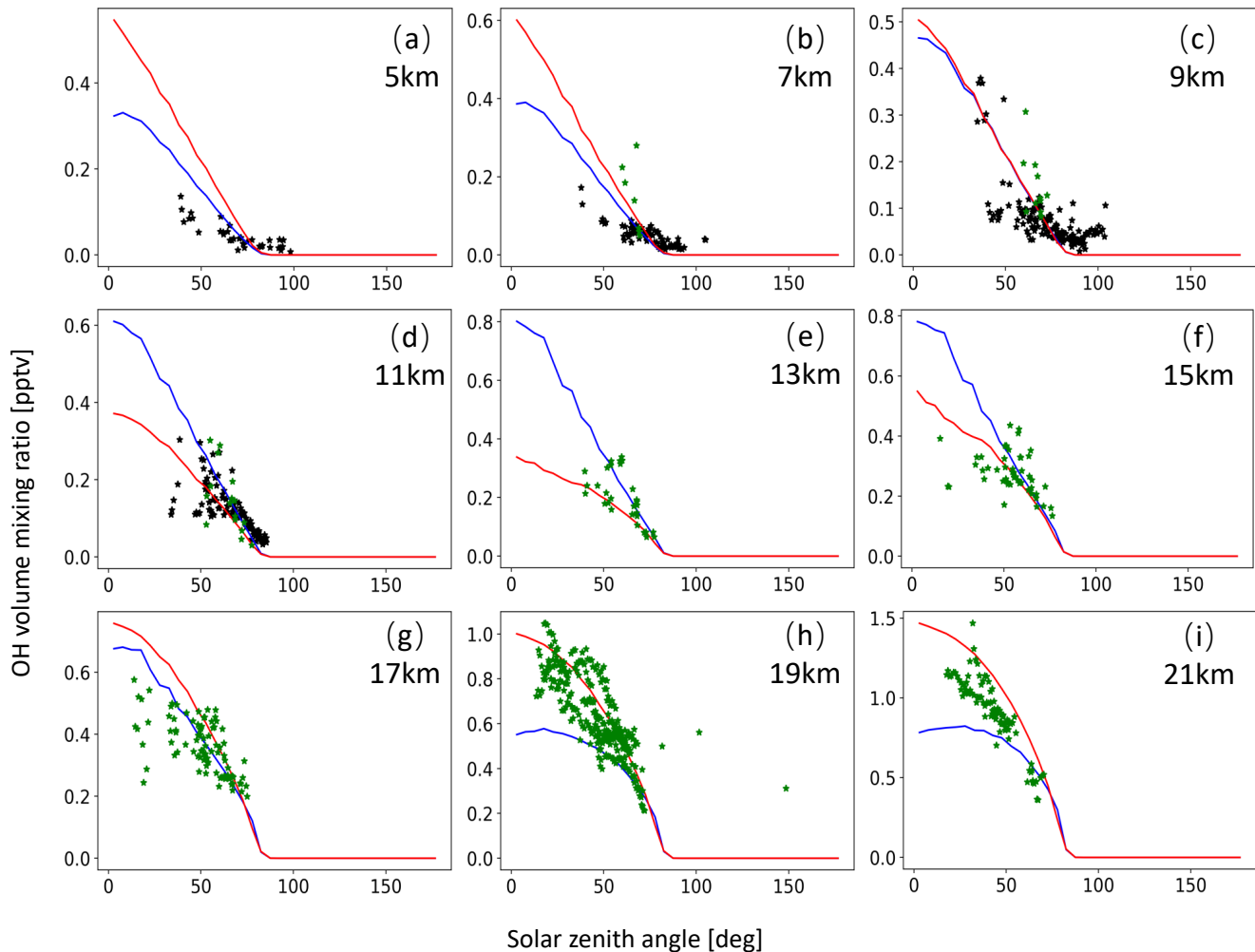
Figure A2. Same as Fig. A1 but for SONEX-DC8 (black points) and MAESA-ER2 (green points) measurements in October.

Competing interests. The authors declare that no competing interests are present.
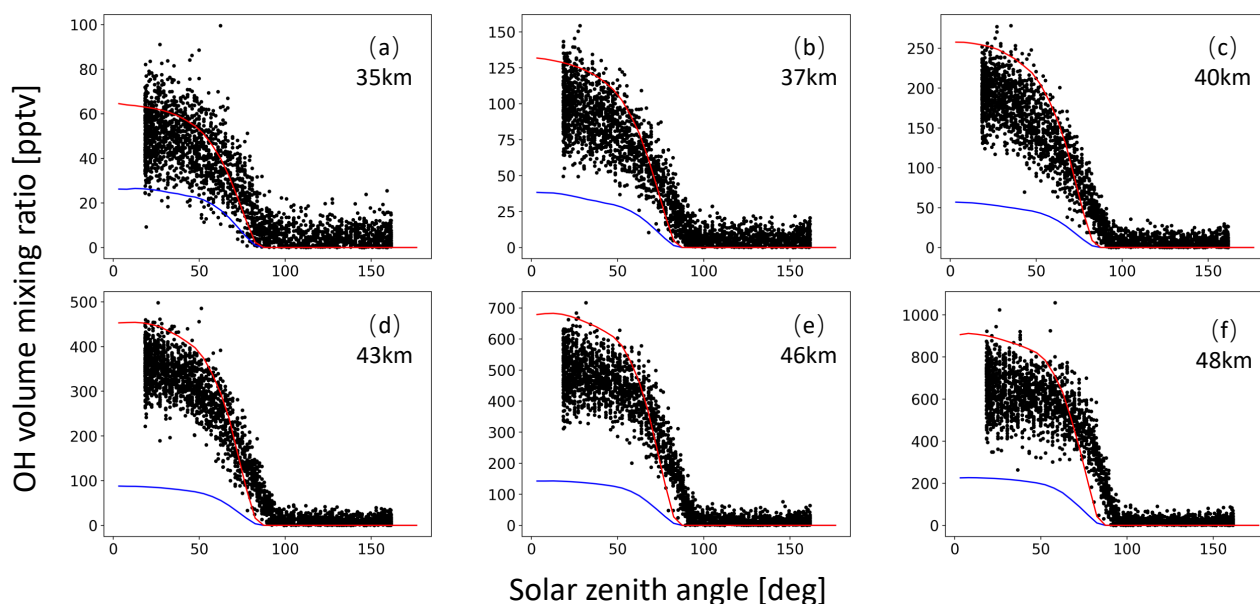
Figure A3. Global average OH volume mixing ratios used in MPTRAC based on predefined monthly mean zonal mean data for the CLaMS model (red curve) and the CAMS reanalysis (blue curve) as well as MLS satellite measurements (black points). The time period being covered is May. Plots in (a) to (f) refer to altitudes of 35, 37, 40, 43, 46, and 48 km, respectively.

References

Aumann, H., Chahine, M., Gautier, C., Goldberg, M., Kalnay, E., McMillin, L., Revercomb, H., Rosenkranz, P., Smith, W., Staelin, D., Strow, L., and Susskind, J.: AIRS/AMSU/HSB on the Aqua mission: design, science objectives, data products, and processing systems, IEEE Trans. Geosci. Remote Sens., 41, 253–264, https://doi.org/10.1109/TGRS.2002.808356, 2003.

Barth, M. C., Hegg, D. A., Hobbs, P. V., Walega, J. G., Kok, G. L., Heikes, B. G., and Lazrus, A. L.: Measurements of atmospheric gas-phase and aqueous-phase hydrogen peroxide concentrations in winter on the east coast of the United States, Tellus, 41B, 61–69, https://doi.org/https://doi.org/10.1111/j.1600-0889.1989.tb00125.x, 1989.

Berglen, T. F., Berntsen, T. K., Isaksen, I. S. A., and Sundet, J. K.: A global model of the coupled sulfur/oxidant chemistry in the troposphere: The sulfur cycle, J. Geophys. Res. Atmos., 109, https://doi.org/https://doi.org/10.1029/2003JD003948, 2004.

Brenot, H., Theys, N., Clarisse, L., van Geffen, J., van Gent, J., van Roozendael, M., van der A, R., Hurtmans, D., Coheur, P. F., Clerbaux, C., Valks, P., Hedelt, P., Prata, F., Rasson, O., Sievers, K., and Zehner, C.: Support to Aviation Control Service (SACS): an online service for near-real-time satellite monitoring of volcanic plumes, Nat. Hazards Earth Syst. Sci., 14, 1099–1123, https://doi.org/10.5194/nhess-14-1099-2014, 2014.

Burkholder, J. B., Sander, S. P., J. Abbatt, J. R. B., Cappa, C., Crounse, J. D., Dibble, T. S., Huie, R. E., Kolb, C. E., Kurylo, M. J., Orkin, V. L., Percival, C. J., Wilmouth, D. M., and Wine, P. H.: Chemical kinetics and photochemical data for use in atmospheric studies: evaluation number 19, Tech. rep., Jet Propulsion Laboratory, Pasadena, http://jpldataeval.jpl.nasa.gov/, 2019.

Cai, Z., Griessbach, S., and Hoffmann, L.: Improved estimation of volcanic SO_2 injections from satellite retrievals and Lagrangian transport simulations: the 2019 Raikoke eruption, Atmos. Chem. Phys., 22, 6787–6809, https://doi.org/10.5194/acp-22-6787-2022, 2022.

500   de Leeuw, J., Schmidt, A., Witham, C. S., Theys, N., Taylor, I. A., Grainger, R. G., Pope, R. J., Haywood, J., Osborne, M., and Kristiansen, N. I.: The 2019 Raikoke volcanic eruption – Part 1: Dispersion model simulations and satellite retrievals of volcanic sulfur dioxide, Atmos. Chem. Phys., 21, 10 851–10 879, https://doi.org/10.5194/acp-21-10851-2021, 2021.

Dee, D. P., Uppala, S. M., Simmons, A. J., Berrisford, P., Poli, P., Kobayashi, S., Andrae, U., Balmaseda, M. A., Balsamo, G., Bauer, P., Bechtold, P., Beljaars, A. C. M., van de Berg, L., Bidlot, J., Bormann, N., Delsol, C., Dragani, R., Fuentes, M., Geer, A. J., Haimberger, L.,

505   Healy, S. B., Hersbach, H., Hólm, E. V., Isaksen, L., Kållberg, P., Köhler, M., Matricardi, M., McNally, A. P., Monge-Sanz, B. M., Morcrette, J.-J., Park, B.-K., Peubey, C., de Rosnay, P., Tavolato, C., Thépaut, J.-N., and Vitart, F.: The ERA-Interim reanalysis: configuration and performance of the data assimilation system, Q. J. R. Meteorol. Soc., 137, 553–597, https://doi.org/https://doi.org/10.1002/qj.828, 2011.

Delmelle, P., Stix, J., Baxter, P., Garcia-Alvarez, J., and Barquero, J.: Atmospheric dispersion, environmental effects and poten-

510   tial health hazard associated with the low-altitude gas plume of Masaya volcano, Nicaragua, Bull. Volcanol., 64, 423–434, https://doi.org/10.1007/s00445-002-0221-6, 2002.

Draxler, R. and Hess, G.: An overview of the HYSPLIT_4 modelling system for trajectories, dispersion and deposition, Austral. Meteo. Mag., 47, 295–308, 1998.

Eatough, D., Caka, F., and Farber, R.: The Conversion of SO2 to Sulfate in the Atmosphere, Isr. J. Chem., 34, 301–314,

515   https://doi.org/https://doi.org/10.1002/ijch.199400034, 1994.

Eckhardt, S., Prata, A. J., Seibert, P., Stebel, K., and Stohl, A.: Estimation of the vertical profile of sulfur dioxide injection into the atmosphere by a volcanic eruption using satellite column measurements and inverse transport modeling, Atmos. Chem. Phys., 8, 3881–3897, https://doi.org/10.5194/acp-8-3881-2008, 2008.

Elperin, T., Fominykh, A., and Krasovitov, B.: Precipitation scavenging of gaseous pollutants having arbitrary solubility in inhomogeneous

520   atmosphere, Meteorol. Atmos. Phys., 127, 205–216, https://doi.org/10.1007/s00703-014-0358-9, 2015.

ESPO: ESPO data archive, https://espoarchive.nasa.gov/archive/browse/, 2022.

Garrett, T. J., Avey, L., Palmer, P. I., Stohl, A., Neuman, J. A., Brock, C. A., Ryerson, T. B., and Holloway, J. S.: Quantifying wet scavenging processes in aircraft observations of nitric acid and cloud condensation nuclei, J. Geophys. Res. Atmos., 111, https://doi.org/10.1029/2006JD007416, 2006.

525   Gerbig, C., Lin, J. C., Wofsy, S. C., Daube, B. C., Andrews, A. E., Stephens, B. B., Bakwin, P. S., and Grainger, C. A.: Toward constraining regional-scale fluxes of CO2 with atmospheric observations over a continent: 2. Analysis of COBRA data using a receptor-oriented framework, J. Geophys. Res. Atmos., 108, https://doi.org/https://doi.org/10.1029/2003JD003770, 2003.

Grooß, J.-U. and Russell III, J. M.: Technical note: A stratospheric climatology for O_3, H_2O, CH_4, NO_x, HCl and HF derived from HALOE measurements, Atmos. Chem. Phys., 5, 2797–2807, https://doi.org/10.5194/acp-5-2797-2005, 2005.

530   Hansell, A. and Oppenheimer, C.: Health hazards from volcanic gases: A systematic literature review, Arch. Environ. Health, 59, 628–639, https://doi.org/10.1080/00039890409602947, 2004.

Heng, Y., Hoffmann, L., Griessbach, S., Roessler, T., and Stein, O.: Inverse transport modeling of volcanic sulfur dioxide emissions using large-scale simulations, Geosci. Model Dev., 9, 1627–1645, https://doi.org/10.5194/gmd-9-1627-2016, 2016.

Hersbach, H., Bell, B., Berrisford, P., Hirahara, S., Horanyi, A., Munoz-Sabater, J., Nicolas, J., Peubey, C., Radu, R., Schepers, D., Simmons,

535   A., Soci, C., Abdalla, S., Abellan, X., Balsamo, G., Bechtold, P., Biavati, G., Bidlot, J., Bonavita, M., De Chiara, G., Dahlgren, P., Dee,

D., Diamantakis, M., Dragani, R., Flemming, J., Forbes, R., Fuentes, M., Geer, A., Haimberger, L., Healy, S., Hogan, R. J., Holm, E., Janiskova, M., Keeley, S., Laloyaux, P., Lopez, P., Lupu, C., Radnoti, G., de Rosnay, P., Rozum, I., Vamborg, F., Villaume, S., and Thepaut, J.-N.: The ERA5 global reanalysis, Q. J. R. Meteorol. Soc., 146, 1999–2049, https://doi.org/10.1002/qj.3803, 2020.

Hoffmann, L. and Spang, R.: An assessment of tropopause characteristics of the ERA5 and ERA-Interim meteorological reanalyses, Atmos. Chem. Phys., 22, 4019–4046, https://doi.org/10.5194/acp-22-4019-2022, 2022.

Hoffmann, L., Griessbach, S., and Meyer, C. I.: Volcanic emissions from AIRS observations: detection methods, case study, and statistical analysis, in: Remote Sensing of Clouds and the Atmosphere XIX; and Optics in Atmospheric Propagation and Adaptive Systems XVII, edited by Comerón, A., Kassianov, E. I., Schäfer, K., Picard, R. H., Stein, K., and Gonglewski, J. D., vol. 9242, p. 924214, International Society for Optics and Photonics, SPIE, https://doi.org/10.1117/12.2066326, 2014.

Hoffmann, L., Baumeister, P. F., Cai, Z., Clemens, J., Griessbach, S., Günther, G., Heng, Y., Liu, M., Haghighi Mood, K., Stein, O., et al.: Massive-Parallel Trajectory Calculations version 2.2 (MPTRAC-2.2): Lagrangian transport simulations on graphics processing units (GPUs), Geosci. Model Dev., 15, 2731–2762, https://doi.org/https://doi.org/10.31223/X52S7M, 2022a.

Hoffmann, L., Clemens, J., Haghighi Mood, K., and Liu, M.: Massive-Parallel Trajectory Calculations (MPTRAC) (v2.4), https://doi.org/10.5281/zenodo.7473222, 2022b.

Hoffmann, L., Roessler, T., Griessbach, S., Heng, Y., and Stein, O.: Lagrangian transport simulations of volcanic sulfur dioxide emissions: Impact of meteorological data products, J. Geophys. Res. Atmos., 121, 4651–4673, https://doi.org/10.1002/2015JD023749, 2016.

Hoffmann, L., Guenther, G., Li, D., Stein, O., Wu, X., Griessbach, S., Heng, Y., Konopka, P., Mueller, R., Vogel, B., and Wright, J. S.: From ERA-Interim to ERA5: the considerable impact of ECMWF's next-generation reanalysis on Lagrangian transport simulations, Atmos. Chem. Phys., 19, 3097–3124, https://doi.org/10.5194/acp-19-3097-2019, 2019.

Höpfner, M., Boone, C. D., Funke, B., Glatthor, N., Grabowski, U., Günther, A., Kellmann, S., Kiefer, M., Linden, A., Lossow, S., Pumphrey, H. C., Read, W. G., Roiger, A., Stiller, G., Schlager, H., von Clarmann, T., and Wissmüller, K.: Sulfur dioxide (SO_2) from MIPAS in the upper troposphere and lower stratosphere 2002–2012, Atmos. Chem. Phys., 15, 7017–7037, https://doi.org/10.5194/acp-15-7017-2015, 2015.

Inness, A., Ades, M., Agusti-Panareda, A., Barre, J., Benedictow, A., Blechschmidt, A.-M., Dominguez, J. J., Engelen, R., Eskes, H., Flemming, J., Huijnen, V., Jones, L., Kipling, Z., Massart, S., Parrington, M., Pench, V.-H., Razinger, M., Remy, S., Schulz, M., and Suttie, M.: The CAMS reanalysis of atmospheric composition, Atmos. Chem. Phys., 19, 3515–3556, https://doi.org/10.5194/acp-19-3515-2019, 2019.

Iribarne, J., Barrie, L., and Iribarne, A.: Effect of freezing on sulfur dioxide dissolved in supercooled droplets, Atmos. Environ., 17, 1047–1050, https://doi.org/https://doi.org/10.1016/0004-6981(83)90287-1, 1983.

Iribarne, J., Pyshnov, T., and Naik, B.: The effect of freezing on the composition of supercooled droplets—II. Retention of S(IV), Atmos. Environ., 24, 389–398, https://doi.org/https://doi.org/10.1016/0960-1686(90)90119-8, 1990.

Jülich Supercomputing Centre: JUWELS: Modular Tier-0/1 Supercomputer at the Jülich Supercomputing Centre, J. Large-scale Res. Facilities, 5, A135, https://doi.org/10.17815/jlsrf-5-171, 2019.

Khokhar, M., Frankenberg, C., Van Roozendael, M., Beirle, S., Kuhl, S., Richter, A., Platt, U., and Wagner, T.: Satellite observations of atmospheric SO2 from volcanic eruptions during the time-period of 1996-2002, Adv. Space Res., 36, 879–887, https://doi.org/10.1016/j.asr.2005.04.114, 2005.

Kloss, C., Sellitto, P., Legras, B., Vernier, J.-P., Jegou, F., Venkat Ratnam, M., Suneel Kumar, B., Lakshmi Madhavan, B., and Berthet, G.: Impact of the 2018 Ambae Eruption on the Global Stratospheric Aerosol Layer and Climate, J. Geophys. Res. Atmos., 125, https://doi.org/10.1029/2020JD032410, 2020.

575 Koch, D., Jacob, D., Tegen, I., Rind, D., and Chin, M.: Tropospheric sulfur simulation and sulfate direct radiative forcing in the Goddard Institute for Space Studies general circulation model, J. Geophys. Res. Atmos., 104, 23 799–23 822, https://doi.org/https://doi.org/10.1029/1999JD900248, 1999.

Krippner, J. and Venzke, E.: Global Volcanism Program, 2019. Report on Ambae (Vanuatu), https://doi.org/10.5479/si.GVP. BGVN201902-257030, 2019.

580 Lamb, D. and Blumenstein, R.: Measurement of the entrapment of sulfur dioxide by rime ice, Atmos. Environ., 21, 1765–1772, https://doi.org/https://doi.org/10.1016/0004-6981(87)90116-8, 1987.

Levine, S. and Schwartz, S.: In-cloud and below-cloud scavenging of Nitric acid vapor, Atmos. Environ., 16, 1725–1734, https://doi.org/https://doi.org/10.1016/0004-6981(82)90266-9, 1982.

Liu, M., Huang, Y., Hoffmann, L., Huang, C., Chen, P., and Heng, Y.: High-Resolution Source Estimation of Volcanic Sulfur Dioxide Emis-
585 sions Using Large-Scale Transport Simulations, in: Computational Science – ICCS 2020, edited by Krzhizhanovskaya, V. V., Závodszky, G., Lees, M. H., Dongarra, J. J., Sloot, P. M. A., Brissos, S., and Teixeira, J., pp. 60–73, Springer International Publishing, 2020.

Maass, F., Elias, H., and Wannowius, K.: Kinetics of the oxidation of hydrogen sulfite by hydrogen peroxide in aqueous solution: ionic strength effects and temperature dependence, Atmos. Environ., 33, 4413–4419, https://doi.org/10.1016/S1352-2310(99)00212-5, 1999.

Malinina, E., Rozanov, A., Niemeier, U., Wallis, S., Arosio, C., Wrana, F., Timmreck, C., von Savigny, C., and Burrows, J. P.: Changes in
590 stratospheric aerosol extinction coefficient after the 2018 Ambae eruption as seen by OMPS-LP and MAECHAM5-HAM, Atmos. Chem. Phys., 21, 14 871–14 891, https://doi.org/10.5194/acp-21-14871-2021, 2021.

Martin, A.: Estimated washout coefficients for sulphur dioxide, nitric oxide, nitrogen dioxide and ozone, Atmos. Environ., 18, 1955–1961, https://doi.org/https://doi.org/10.1016/0004-6981(84)90373-1, cACGP Symposium on Tropospheric Chemistry With Emphasis on Sulphur and Nitrogen Cycles and the Chemistry of Clouds and Precipitation, 1984.

595 Maul, P.: Preliminary estimates of the washout coefficient for sulphur dioxide using data from an east midlands ground level monitoring network, Atmos. Environ., 12, 2515–2517, https://doi.org/https://doi.org/10.1016/0004-6981(78)90298-6, 1978.

McGonigle, A. J. S., Delmelle, P., Oppenheimer, C., Tsanev, V. I., Delfosse, T., Williams-Jones, G., Horton, K., and Mather, T. A.: SO2 depletion in tropospheric volcanic plumes, Geophys. Res. Lett., 31, https://doi.org/https://doi.org/10.1029/2004GL019990, 2004.

Minschwaner, K., Manney, G. L., Wang, S. H., and Harwood, R. S.: Hydroxyl in the stratosphere and mesosphere - Part 1: Diurnal variability,
600 Atmos. Chem. Phys., 11, 955–962, https://doi.org/10.5194/acp-11-955-2011, 2011.

Moussallam, Y., Rose-Koga, E. F., Koga, K. T., Medard, E., Bani, P., Devidal, J.-L., and Tari, D.: Fast ascent rate during the 2017-2018 Plinian eruption of Ambae (Aoba) volcano: a petrological investigation, Contrib. to Mineral. Petrol., 174, https://doi.org/10.1007/s00410-019-1625-z, 2019.

Pattantyus, A. K., Businger, S., and Howell, S. G.: Review of sulfur dioxide to sulfate aerosol chemistry at Kilauea Volcano, Hawai'i, Atmos.
605 Environ., 185, 262–271, https://doi.org/10.1016/j.atmosenv.2018.04.055, 2018.

Pisso, I., Sollum, E., Grythe, H., Kristiansen, I, N., Cassiani, M., Eckhardt, S., Arnold, D., Morton, D., Thompson, R. L., Zwaaftink, C. D. G., Evangeliou, N., Sodemann, H., Haimberger, L., Henne, S., Brunner, D., Burkhart, J. F., Fouilloux, A., Brioude, J., Philipp, A., Seibert, P., and Stohl, A.: The Lagrangian particle dispersion model FLEXPART version 10.4, Geosci. Model Dev., 12, 4955–4997, https://doi.org/10.5194/gmd-12-4955-2019, 2019.

610 Pommrich, R., Mueller, R., Grooss, J. U., Konopka, P., Ploeger, F., Vogel, B., Tao, M., Hoppe, C. M., Guenther, G., Spelten, N., Hoffmann, L., Pumphrey, H. C., Viciani, S., D'Amato, F., Volk, C. M., Hoor, P., Schlager, H., and Riese, M.: Tropical troposphere to stratosphere transport of carbon monoxide and long-lived trace species in the Chemical Lagrangian Model of the Stratosphere (CLaMS), Geosci. Model Dev., 7, 2895–2916, https://doi.org/10.5194/gmd-7-2895-2014, 2014.

Redington, A. L., Derwent, R. G., Witham, C. S., and Manning, A. J.: Sensitivity of modelled sulphate and nitrate aerosol to cloud, pH and
615 ammonia emissions, Atmos. Environ., 43, 3227–3234, https://doi.org/10.1016/j.atmosenv.2009.03.041, 2009.

Robock, A.: Volcanic eruptions and climate, Rev. Geophys., 38, 191–219, https://doi.org/10.1029/1998RG000054, 2000.

Rolph, G., Draxler, R., and Depena, R.: Modeling Sulfur Concentrations and Depositions in the United-States During Anatex, Atmos. Environ., 26, 73–93, https://doi.org/10.1016/0960-1686(92)90262-J, 1992.

SACS: Support to Aviation Control Service, https://sacs.aeronomie.be, 2022.

620 Sander, R.: Compilation of Henry's law constants (version 4.0) for water as solvent, Atmos. Chem. Phys., 15, 4399–4981, https://doi.org/10.5194/acp-15-4399-2015, 2015.

Schmidt, A., Ostro, B., Carslaw, K. S., Wilson, M., Thordarson, T., Mann, G. W., and Simmons, A. J.: Excess mortality in Europe following a future Laki-style Icelandic eruption, Proc. Natl. Acad. Sci. U.S.A., 108, 15 710–15 715, https://doi.org/10.1073/pnas.1108569108, 2011.

Slinn, W. G. N.: Rate-Limiting Aspects of In-Cloud Scavenging, J. Atmos. Sci., 31, 1172 – 1173, https://doi.org/10.1175/1520-
625 0469(1974)031<1172:RLAOIC>2.0.CO;2, 1974.

Stuart, A. L. and Jacobson, M.: A numerical model of the partitioning of trace chemical solutes during drop freezing, J. Atmos. Chem., 53, 13–42, 2006.

Theys, N., De Smedt, I., Yu, H., Danckaert, T., van Gent, J., Hoermann, C., Wagner, T., Hedelt, P., Bauer, H., Romahn, F., Pedergnana, M., Loyola, D., and Van Roozendael, M.: Sulfur dioxide retrievals from TROPOMI onboard Sentinel-5 Precursor: algorithm theoretical basis,
630 Atmos. Meas. Tech., 10, 119–153, https://doi.org/10.5194/amt-10-119-2017, 2017.

Theys, N., Romahn, F., and Wagner, T.: S5P Mission Performance Centre Sulphur Dioxide Readme, https://sentinel.esa.int/documents/247904/3541451/Sentinel-5P-Sulphur-Dioxide-Readme.pdf, 2020.

Veefkind, J., Aben, I., McMullan, K., Förster, H., de Vries, J., Otter, G., Claas, J., Eskes, H., de Haan, J., Kleipool, Q., van Weele, M., Hasekamp, O., Hoogeveen, R., Landgraf, J., Snel, R., Tol, P., Ingmann, P., Voors, R., Kruizinga, B., Vink, R., Visser, H., and Levelt,
635 P.: TROPOMI on the ESA Sentinel-5 Precursor: A GMES mission for global observations of the atmospheric composition for climate, air quality and ozone layer applications, Remote Sens. Environ., 120, 70–83, https://doi.org/https://doi.org/10.1016/j.rse.2011.09.027, the Sentinel Missions - New Opportunities for Science, 2012.

Webster, H. and Thomson, D.: The NAME wet deposition scheme, https://library.metoffice.gov.uk/Portal/Default/en-GB/RecordView/Index/197129, 2014.

640 Wu, X., Griessbach, S., and Hoffmann, L.: Long-range transport of volcanic aerosol from the 2010 Merapi tropical eruption to Antarctica, Atmos. Chem. Phys., 18, 15 859–15 877, https://doi.org/10.5194/acp-18-15859-2018, 2018.

Wu, X., Griessbach, S., and Hoffmann, L.: Equatorward dispersion of a high-latitude volcanic plume and its relation to the Asian summer monsoon: a case study of the Sarychev eruption in 2009, Atmos. Chem. Phys., 17, 13 439–13 455, https://doi.org/10.5194/acp-17-13439-2017, 2017.